**The Thesis Committee for David McLean Wiggs**
**Certifies that this is the approved version of the following Thesis:**

# A Generalized Model to Estimate the Elastic Stiffness Tensor of Mudrocks Based on the Full Strain Tensor

**APPROVED BY**
**SUPERVISING COMMITTEE:**

Peter B. Flemings, Supervisor

Kyle T. Spikes

Maria A. Nikolinakou

# A Generalized Model to Estimate the Elastic Stiffness Tensor of Mudrocks Based on the Full Strain Tensor

**by**

**David McLean Wiggs**

**Thesis**

Presented to the Faculty of the Graduate School of

The University of Texas at Austin

in Partial Fulfillment

of the Requirements

for the Degree of

**Master of Science in Geological Sciences**

**The University of Texas at Austin**

**May 2021**

## Acknowledgements

First, I would like to thank my advisor, Peter Flemings. He pushed me to not be satisfied with a partial solution and made me a better scientist and person. Thank you for always expecting excellence. No matter my future endeavors, you have prepared me with the proper mindset. I would also like to thank my committee members, Kyle Spikes and Maria Nikolinakou. They have been heavily involved throughout my research and lent their hand at every challenge in my research. Thank you for taking the time to deal with my countless questions.

I would also like to thank the entire GeoFluids group. Thank you, Dr. Germaine, for your lighthearted and unique problem-solving approach. Thank you, Felicia and Lynda, for constantly juggling my schedule and fitting me in for any reason. I would also like to thank Philip Guerrero for his help in navigating my graduate degree. In addition, I would like to express gratitude provided the generous financial support of: the Geofluids Consortium and its sponsors Shell, Hess, Tufts, ConoccoPhillips, BP, Oxy, BHP, ExxonMobil, Chevron, Petrobras, and The University of Texas at Austin.

Next, I would like to thank my parents, Brett and Alesia Wiggs. Thank you for supporting me in every pursuit and leading by example. I dream to follow in each of your steps and hope to obtain even a fraction of your accomplishments. I also would like to thank my roommates, Harry Hull, Jake Gearon, and John Franey. I am grateful to have lived with such exceptional geoscientists and can't wait to see how our futures will align. Each of you was a constant source of ideas and brought my research to new heights. Finally, I would like to thank Jacqueline Fatjo. Thank you for cheering me on in all endeavors and lending an ear to me at all times.

# Abstract


## A Generalized Model to Estimate the Elastic Stiffness Tensor of Mudrocks Based on the Full Strain Tensor



David McLean Wiggs, M.S. Geo. Sci.

The University of Texas at Austin, 2021

Supervisor: Peter B. Flemings



I develop a three-step framework to model the anisotropic elastic properties of a mechanically compacted mudrock based on the full strain tensor. I model the microstructure as an effective medium representative of locally aligned domains of clay grains and fluid filled porosity with isolated quartz. Then I predict the orientation of these building blocks due to the application of any strain field. Finally, the previous two steps are combined to determine an effective medium model for the entire mudrock that predicts the elastic stiffness matrix. I focus on the relationship of deformation to porosity reduction and grain alignment in mudrocks. My results show that the application of axial loading leads to the development of elastic anisotropy with stiffnesses increasing more rapidly in the direction perpendicular to loading. These stiffness predictions closely match experimental data on a mudrock specimen from Eugene Island – Gulf of Mexico. I further apply my three-step framework to predict elastic stiffnesses in a synthetic salt basin based on the full strain tensor predicted by an evolutionary poromechanical model.

This coupling allows us to predict elastic stiffnesses and anisotropy due to sediment deposition and non-uniaxial salt loading. Accurate estimation of elastic stiffnesses for mudrocks based on the full strain tensor holds immense potential to improve pressure prediction, seismic imaging in complex geologic environments, and prospect evaluation.

# Table of Contents

## List of Tables

# List of Figures

# CHAPTER 1: INTRODUCTION

## 1.1 OBJECTIVES

Mudrocks have been understudied relative to sandstones and carbonates in the past despite comprising 75% of sedimentary fill of basins (Jones and Wang, 1981). Reasons for the lack of investigation include their inherent lithologic and mechanical variability along with their previously unrecoverable resources prior to the unconventional revolution (Jones and Wang, 1981; Pervukhina et al., 2015). Interest in mudrocks has increased due to their development as unconventional resource plays.

The objective of this work is to predict the elastic stiffness matrix of a mudrock as a function of the deformation the rock has undergone based on grain reorientation and porosity reduction. The prediction of these properties provides the ability to enhance seismic imaging, to interpret deformation, and to identify potential hydrocarbon reservoirs. The result holds several specific potential applications. First, the combination of my workflow with a poromechanical model allows for an investigation of the impact of any deformation on the elastic properties of mudrocks. Second, the workflow combined with inverse methods could be used to assess stress and deformation in field data. Finally, my workflow along with tilted transverse isotropic (TTI) seismic processing techniques could provide for an improvement of seismic imaging methods. My workflow could improve seismic processing due to the integration of principal strain orientation versus the definition of the tilt angle according to dip. The workflow provided in this thesis gives a framework to investigate and predict the impact of any deformation on the elastic properties.

## 1.2 CHAPTER DESCRIPTIONS

In Chapter 2, I present a rock-physics modeling approach to predict the full elastic stiffness matrix and anisotropy of mechanically compacted mudrocks based on the full strain tensor. First, I construct an effective medium of a constant volume composed of clay, quartz, and porosity through the combination of the anisotropic Self-Consistent Approximation (SCA) and Differential Effective medium (DEM). Next, I describe the alignment of building blocks as a function of deformation with the March Model (March, 1932). I examine two types of deformation (uniaxial compaction and pure shear) to illustrate building block alignment. In uniaxial compaction, the vertical component of strain is nonzero, while all others are zero. In pure shear deformation, the vertical component of strain corresponds to an equal but opposite change in the horizontal component. The other horizontal axis remains equal to zero, and the third is zero. Finally, I combine the previous two steps through a Voigt approximation to determine the mudrock elastic stiffnesses. The uniaxial compaction results are compared to experimental results from Nihei et al. (2011) and Ranjpour (2020). Last, my work is combined with poromechanical model results from (Nikolinakou et al., 2016) to show a potential application of the workflow to large scale complex geologic systems. A portion of this work was presented in the Annual SEG Conference (Wiggs et al., 2020) and Chapter 2 will be submitted as a publication to Geophysics.

Appendices in Chapter 3 provide additional detail on how to replicate the workflow discussed in Chapter 2. The appendices include A) a derivation of the March-Owens ODF to predict the alignment of grains from the full strain tensor and B) determination of the Legendre Coefficients to calculate the elastic properties of a mudrock.

# CHAPTER 2: A GENERALIZED MODEL TO ESTIMATE THE ELASTIC STIFFNESS TENSOR OF MUDROCKS BASED ON THE FULL STRAIN TENSOR


## ABSTRACT

I develop a three-step framework to model the anisotropic elastic properties of a mechanically compacted mudrock based on the full strain tensor. I model the microstructure as an effective medium representative of locally aligned domains of clay grains and fluid-filled porosity with isolated quartz. Then I predict the orientation of these building blocks due to the application of any strain field. Finally, the previous two steps are combined to determine an effective medium model for the entire mudrock that predicts the elastic stiffness matrix. I focus on the relationship of deformation to porosity reduction and grain alignment in mudrocks. My results show that the application of axial loading leads to the development of elastic anisotropy with stiffnesses increasing more rapidly in the direction perpendicular to loading. These stiffness predictions closely match experimental data on a mudrock specimen from Eugene Island – Gulf of Mexico. I further apply my three-step framework to predict elastic stiffnesses in a synthetic salt basin based on the full strain tensor predicted by an evolutionary poromechanical model. This coupling allows us to predict elastic stiffnesses and anisotropy due to sediment deposition and non-uniaxial salt loading. Accurate estimation of elastic stiffnesses for

mudrocks based on the full strain tensor holds immense potential to improve pressure prediction, seismic imaging in complex geologic environments, and prospect evaluation.

## 2.1 INTRODUCTION

Mudrocks experience complex strains during deformation. Platy grains within mudrocks become aligned during applied deformation and this results in the development of elastic anisotropy. For example, the velocity in the direction of alignment is greater than that normal to the alignment. This type of anisotropy, termed grain orientation-induced, is different from other causes of elastic anisotropy such as that caused by layering of different isotropic materials (Backus, 1962) or the closing of cracks normal to the direction of applied stress (Nur and Simmons, 1969; Sayers et al., 2002).

Understanding how elastic stiffnesses evolve as a function deformation is important because stiffnesses are a fundamental input to seismic imaging. Conventional seismic processing typically assumes either that the symmetry axis varies with depth and is vertical (transverse isotropic) or perpendicular to the direction of dip (tilted transverse isotropic (TTI) (Alkhalifah, 2000). This approach does not incorporate the anisotropy that can result from a complex stress field where the symmetry axis is not perpendicular to bedding and might not vary only as a function of depth.  This situation can lead to errors in normal moveout correction, dip moveout correction, seismic migration, and amplitude with variation offset analyses in geologic areas of high deformation due to rotation of the symmetry axis based on the full strain tensor. The error propagates into normal-moveout correction, seismic migration, and amplitude preservation. Proper consideration of the impact of deformation on seismic anisotropy may improve seismic imaging. Furthermore, analysis of seismic velocity anisotropy from seismic data might allow us to invert the state of pressure, stress and deformation from seismic data.

Mudrocks are primarily composed of connected pores filled with fluid, platy clay minerals, and quasi-spherical silt grains (commonly quartz). In Figure 1, platy clay grains have a range of orientations. However, locally, there are clusters of aligned clay grains. Previous studies refer to these local parallel alignment of clay particles as a domain (Red box in Figure 1; Figure 2) (Aylmore and Quirk, 1959).

Multiple studies have modeled the elastic stiffness matrix of domains that include aligned platy particles, pores and grains (Bayuk et al., 2007; Hornby et al., 1994; Sayers, 2005; Vasin et al., 2013). The elastic properties, volume fraction, shape, orientation, and connection of each constituent controls the effective properties of the composite solid (Hornby et al., 1994).

When mudrocks are deposited, the domains containing aligned platy minerals are generally randomly aligned. As the mudrock undergoes uniaxial strain, the domains align (compare Fig. 1a to 1b). Bandyopadhyay (2009) and Johansen et al. (2004) have developed models to describe the elastic stiffness and the anisotropy for a distribution of differently aligned domains due to uniaxial compaction.

I introduce an approach to compute the elastic stiffness of a mudrock for any strain imposed subsequent to deposition. I first compute the elastic stiffness matrix of a building block of aligned grains, porosity, and spherical silt. I next compute the distribution of the alignment of these building blocks for a given deformation. I then compute the elastic stiffness matrix of the aggregate of these building blocks based on the alignment due to deformation. I apply this approach to describe the elastic stiffness matrix across a model of a salt basin. The input is the full strain tensor from a poromechanical model. The output is a complex tilted transversely isotropic (TTI) medium where the orientation aligns to the principal strain tensor not bedding and does not increase systematically with depth.

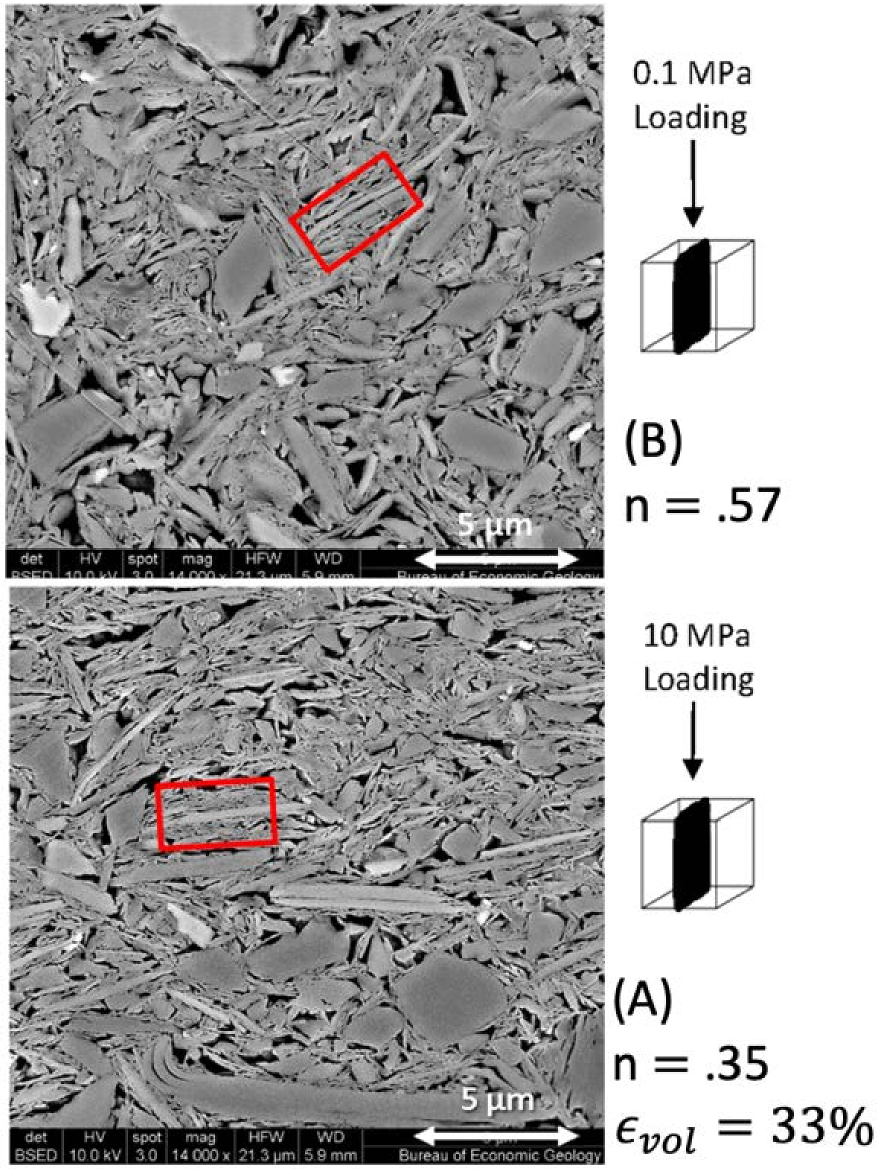


Figure 1: Back scattered electron microscopy (BSEM) images of Resedimented Boston Blue Clay loaded to a vertical effective stress of (A) 0.1 MPa and (B) 10.0 MPa (Emmanuel and Day-Stirrat, 2012). (A) Platy clay grains are approximately randomly oriented with a porosity (n) equal to .57 (Adams et al., 2013). (B) At higher vertical effective stress porosity has decreased following uniaxial compaction and there is alignment of the platy clay grains parallel to the horizontal axis. In this paper, I refer to domains as regions of locally aligned platy clay grains and pores such as are illustrated with the red box. Both images are of a vertical plane parallel to the axial loading direction.

## 2.2 METHODS AND RESULTS

I assume an initially isotropic medium composed of randomly oriented building blocks. The blocks are composed of a domain of aligned platy clay grains and water-filled pores along with isolated spherical quartz grains (Figure 1 and 2). I model the elastic stiffness tensor of these building blocks for any porosity (Figure 3 and 4). I then assume a statistical distribution of the orientation of these building blocks, impose a strain history, and predict the evolution of the orientation of the domains by using the March Model (Figure 6 and 7) (March, 1932). I then combine the building blocks according to the predicted distribution and describe the elastic stiffness behavior with an effective medium model for a mudrock that has undergone any strain history (Figure 8, 9, 10, and 11). The workflow is then applied to generate elastic stiffness matrices across a salt basin based on the full strain tensor from a poromechanical model (Figure 13).

### 2.2.1 Building Block Creation

I model the elastic stiffness tensor for a constant volume element (which I term a building block) composed of water (pore space), clay, and quartz. In successive steps, I add water, silt, or clay while simultaneously removing an equivalent volume of the host medium to arrive at an approximation of the elastic stiffnesses for a mixture a clay and quartz at a particular porosity. I do this in a stepwise fashion. First, I create an effective medium for a building block composed of equal fractions of biconnected aligned platy clay grains and water filled pore space (Figure 2A). Second, I adjust the porosity of the building block while maintaining connectivity of the clay and porosity. (Figure 2B).

Third, I add isolated quartz to the building block (Figure 2C). I then describe the entire building block as an equivalent homogenous effective medium.

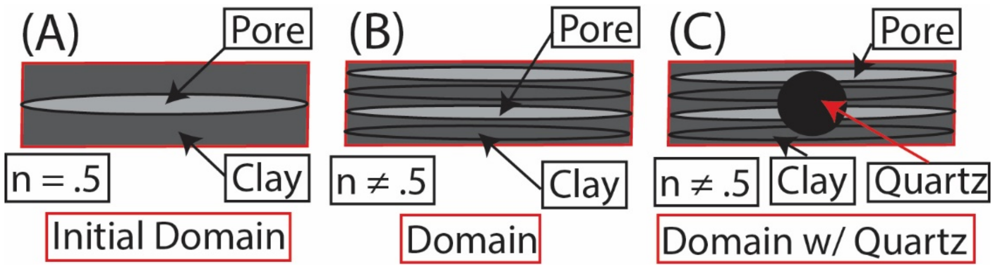


Figure 2: Cartoon depictions of each step to create the building block for my model of a domain with isolated quartz. (A) Initial equal concentration (50% porosity and 50% clay) domain (B) domain at any porosity with additional inclusions and (C) domain at the any porosity with isolated quartz.

The initial building block is assumed to be composed only of equal fractions of clay and porosity that are biconnected. This bi-connectivity allows flow through connected pores, while allowing the solid phase to form a load-bearing skeleton (Jakobsen et al., 2000). This initial building block is described as an effective medium with the anisotropic Self-Consistent Approximation (SCA) (Hornby et al., 1994) (Figure 2A). In the anisotropic SCA, both clay and fluid-filled porosity are introduced together to compute the properties of the effective medium. The effective elastic stiffness tensor ($\underline{c}_{sca}$) for the initial domain is:

$$c_{sca} = [.5c_{clay}Q_{clay} + .5c_{fluid}Q_{fluid}][.5Q_{clay} + .5Q_{fluid}]^{-1} \tag{1}$$

where

$$Q_{clay} = \left[I + G(c_{sca})\left(c_{fluid} - c_{sca}\right)\right]^{-1} \tag{2}$$

and

$$Q_{fluid} = \left[I + G(c_{sca})\left(c_{fluid} - c_{sca}\right)\right]^{-1}. \tag{3}$$

Equation 1 was developed by Willis (1977). $c_{clay}$ and $c_{fluid}$ are the elastic stiffness matrices of the clay and porosity, respectively, *I* is the identity matrix,

$$I = \begin{bmatrix} 1 & 0 & 0 & 0 & 0 & 0 \\ 0 & 1 & 0 & 0 & 0 & 0 \\ 0 & 0 & 1 & 0 & 0 & 0 \\ 0 & 0 & 0 & 1 & 0 & 0 \\ 0 & 0 & 0 & 0 & 1 & 0 \\ 0 & 0 & 0 & 0 & 0 & 1 \end{bmatrix}, \tag{4}$$

and *G* is the calculated geometric strain concentration factor for an ellipsoidal inclusion. Appendix 2 presents the solution of *G* following Bandyopadhyay (2009). *G* depends upon the input elastic stiffness matrix (in this case my original guess at $c_{sca}$) and the dimensions of the spheroidal inclusion. In my work I assume an aspect ratio of 1/10 because the clay and fluid-filled porosity are thin and elongated. The term 0.5 in Eq. 1 reflects the porosity of the initial medium (n=0.5). Equation 1 is solved iteratively with an initial guess for $c_{sca}$. I initially set each matrix value to the average of the corresponding clay and fluid-filled porosity values and compute *G*. The procedure is repeated until $c_{sca}$ converges to a fixed value.

The effective medium that describes the initial building block is next adjusted to reflect elastic properties at any porosity. I use the anisotropic Differential Effective Medium (DEM) (Bandyopadhyay, 2009; Jakobsen et al., 2000) (Figure 2B). The DEM preserves connectivity of any phase that is connected in the initial host medium. The effective elastic stiffness matrix ($c_{dem}$) for any porosity is computed by successively removing an infinitesimal subvolume of host material (composed of clay and pores) and replacing it with a corresponding subvolume of either solely clay (to reduce porosity) or solely fluid (to increase porosity). The replacement of the host material maintains the original volume of the element. The change in stiffness $dc_{dem}$ due to an increase in clay volume (and decrease in porosity) is:

$$dc_{dem} = c_{dem(i+1)} - c_{dem(i)} = \frac{dv_{clayadd}}{1-v_{clayadd}}\left(c_{clay} - c_{dem(i)}\right)Q_{clay}. \tag{5}$$

$Q_{clay}$ is given by equation 2 and $v_{clayadd}$ is the amount of the host medium replaced by clay. The replacement of the host medium by clay means that the total volume will always stay the same, $v_{total} = v_{hostrem} + v_{clayadd} = v_{host}$. Any addition of clay, $v_{clayadd}$, corresponds to an equal removal of original host medium, $v_{host}$, leaving the volume of host remaining, $v_{hostrem}$. In the initial calculation of equation 5, $c_{dem(i)}$ equals $c_{sca}$ as derived from equation 1. The step prior to each calculation will become the host medium for every step after the initial calculation. The porosity of the effective medium that results from equation 5 is:

$$n_{dem} = .5 * (1 - v_{clayadd}) = .5 * v_{hostrem} \tag{6}$$

The change in stiffness $dc_{dem}$ due to an increase in the porosity is:

$$dc_{dem} = c_{dem(i+1)} - c_{dem(i)} = \frac{dv_{fluidadd}}{1-v_{fluidadd}}\left(c_{fluid} - c_{dem(i)}\right)Q_{fluid}, \tag{7}$$

where $Q_{fluid}$ is given by equation 3 and $v_{fluid}$ is the amount of host medium replaced by fluid filled porosity. The replacement of the host medium by porosity means that the total volume will always stay the same, $v_{total} = v_{hostrem} + v_{fluidadd} = v_{host}$. Any addition of porosity, $v_{fluidadd}$, corresponds to an equal removal of original host medium, $v_{host}$, leaving the volume of host remaining, $v_{hostrem}$. The porosity of the effective medium that results from equation 7 is:

$$n_{dem} = .5 * (1 - v_{fluidadd}) + v_{fluidadd} = .5 * v_{hostrem} + v_{fluidadd}. \tag{8}$$

Once the elastic properties for all clay to fluid filled porosity fractions are computed, quartz is added to the biconnected medium through the anisotropic DEM (Figure 2C). I model the quartz as isolated, isotropic quartz grains. To introduce the quartz as isolated grains I take advantage of the fact that any inclusion not represented in the original host will not become connected even if added to high concentrations. When I add quartz, I remove an equivalent volume of the host medium composed of porosity and clay. The change in stiffness $dc_{dem}$ due to an increase in volume of quartz, $dv_{quartzadd}$ is:

$$dc_{dem} = c_{dem(i+1)} - c_{dem(i)} = \frac{dv_{quartzadd}}{1-v_{quartzadd}}\left(c_{quartz} - c_{dem(i)}\right)Q_{quartz}. \quad (9)$$

Where,

$$Q_{quartz} = \left[I + G(c_{sca})\left(c_{quartz} - c_{sca}\right)\right]^{-1}, \quad (10)$$

the initial $c_{dem}$ is equal to the result from equations 5 and 7 and $v_{quartzadd}$ is the amount of the effective medium (both porosity and clay) replaced by quartz. The replacement of the host medium by quartz means that the total volume will always stay the same, $v_{total} = v_{hostrem} + v_{quartzadd} = v_{host}$. Any addition of quartz, $v_{quartzadd}$, corresponds to an equal removal of original host medium, $v_{host}$, leaving the volume of host remaining, $v_{hostrem}$. The effective medium porosity after the introduction of quartz is:

$$n_{buildingblock} = n_{dem} * \left(1 - v_{quartzadd}\right) = n_{dem}v_{hostrem}. \quad (11)$$

The elastic properties of the building block are dependent upon the fraction of clay, quartz, and fluid-filled porosity. The building block is transversely isotropic (TI) with aligned platy clay grains and pores along with isolated quartz. The resulting elastic stiffness matrix is related to the deformation undergone by a mudrock through porosity reduction.

### 2.2.2 Building Block Elastic Stiffnesses

I next illustrate how the elastic stiffnesses of a building block changes as a function of porosity and lithologic composition. The elastic properties for each constituent are taken from (Mavko et al., 2009) (Table 2). All 5 terms of the TI elastic stiffness matrix $(c_{11}, c_{33}, c_{44}, c_{66}, c_{13})$ increase as porosity reduces (Figure 3a and 4a).

The three Thomsen (1986) parameters are:

$$\epsilon = \frac{c_{11} - c_{33}}{2c_{33}} \tag{12}$$

$$\gamma = \frac{c_{66} - c_{44}}{2c_{44}} \tag{13}$$

$$\delta = \frac{(c_{13} + c_{44})^2 - (c_{33} - c_{44})^2}{2c_{33}(c_{33} - c_{44})}. \tag{14}$$

$\epsilon$ is a measure of the anisotropy in the compressional stiffness whereas $\gamma$ is a measure of the anisotropy in shear stiffness. $\epsilon$ begins at nearly isotropic conditions at the initial porosity (n = .57). $\gamma$ is large ($\gamma$ =~3.5, Fig. 3B) because $c_{44}$ (the vertical elastic stiffness) is very small ($c_{44}$= ~.1) relative to the horizontal elastic stiffness ($c_{66}$ =~1 to 4) (Figure 3A). The vertical stiffness is small because horizontally aligned ellipsoidal are very weak (Figure 3B and 4B). As porosity decreases (moving from left to right in Figure 3B and 4B), both the compressional and shear stiffnesses develop anisotropy as seen by the corresponding rise in $\epsilon$ and $\gamma$. $\gamma$ increases until it reaches as maximum value of 4.5 at 42% porosity. Continued porosity reduction leads to higher fractions of bulk rock that reduce the impact of pore shape on the shear anisotropy, $\gamma$. $\delta$ remains near zero at all porosities.

I also examine the impact of changing the volume fraction of clay and quartz from 65% and 35% (Figure 3) to 25% and 75% (Figure 4). The difference between the two lithologies elastic stiffness matrices and associated elastic anisotropy is plotted in Figure 5. The largest differences between any elastic stiffness occurs at n = .45 with a 1 GPa difference in $c_{11}$ (Figure 5). Comparing this to the impact of changing porosity, I see a 9 GPa change of, $c_{11}$, from n = .57 to n = .3 (Figure 3). The porosity of the building block dominates the change in magnitude of the elastic stiffness matrix because the pores are the easiest to deform due to their elongate shape and the large difference in elastic properties of the fluid filled porosity vs either clay or quartz (Table 2). For Thomsen's parameters, $\epsilon$ remains within 0.1 between the quartz fractions (Figure 5B). However, $\gamma$ is almost double for the higher clay fraction case vs the higher quartz fraction case at all porosities. The higher shear anisotropy in the higher clay fraction is explained as follows. $c_{44}$, the minimum shear stiffness approaches zero because of the thin ellipsoidal shape of the clay grains vs the circular shape of quartz grains. The introduction of quartz reduces the shear anisotropy of the building block because it has isotropic characteristics and a shear modulus that is an order of magnitude higher then clay or fluid-filled porosity.

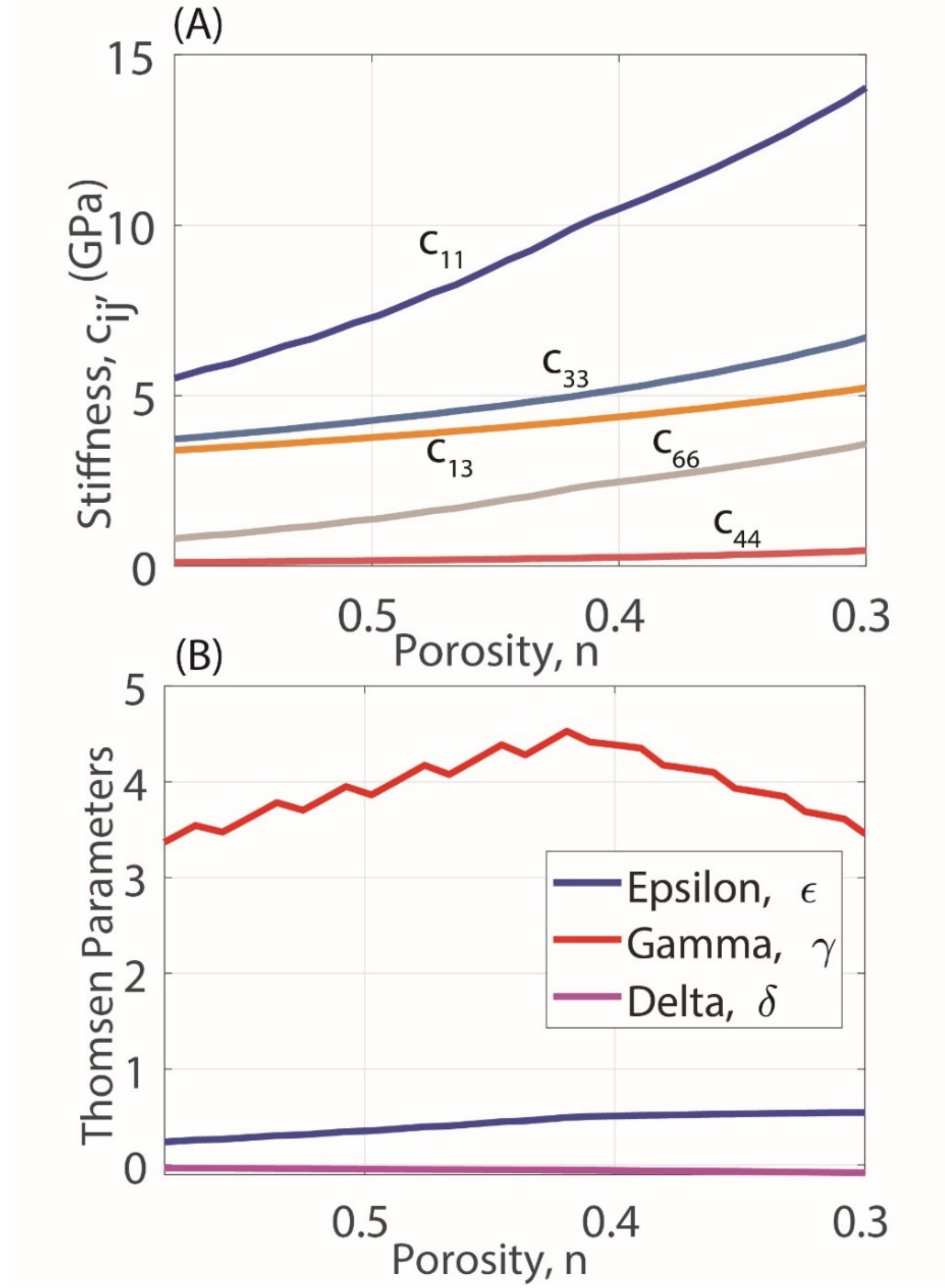


Figure 3: Transversely Isotropic (TI) effective elastic stiffness matrix of a building block vs porosity. The bulk rock composition is 65% clay and 35% quartz.

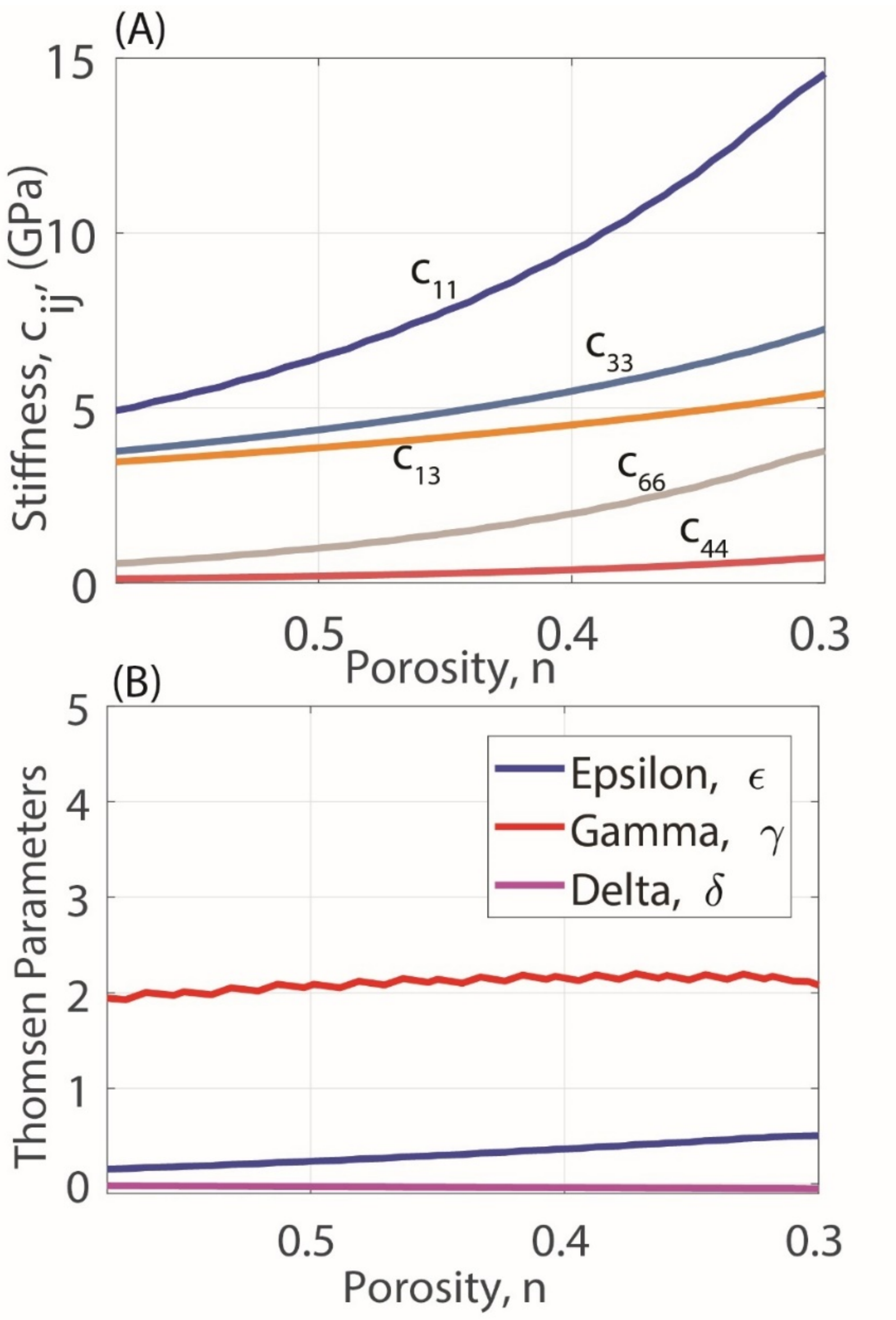


Figure 4: (A) Transversely Isotropic (TI) effective elastic stiffness matrix of a building block (B) Thomsen' parameters vs porosity. The bulk rock composition is 25% clay and 75% quartz.

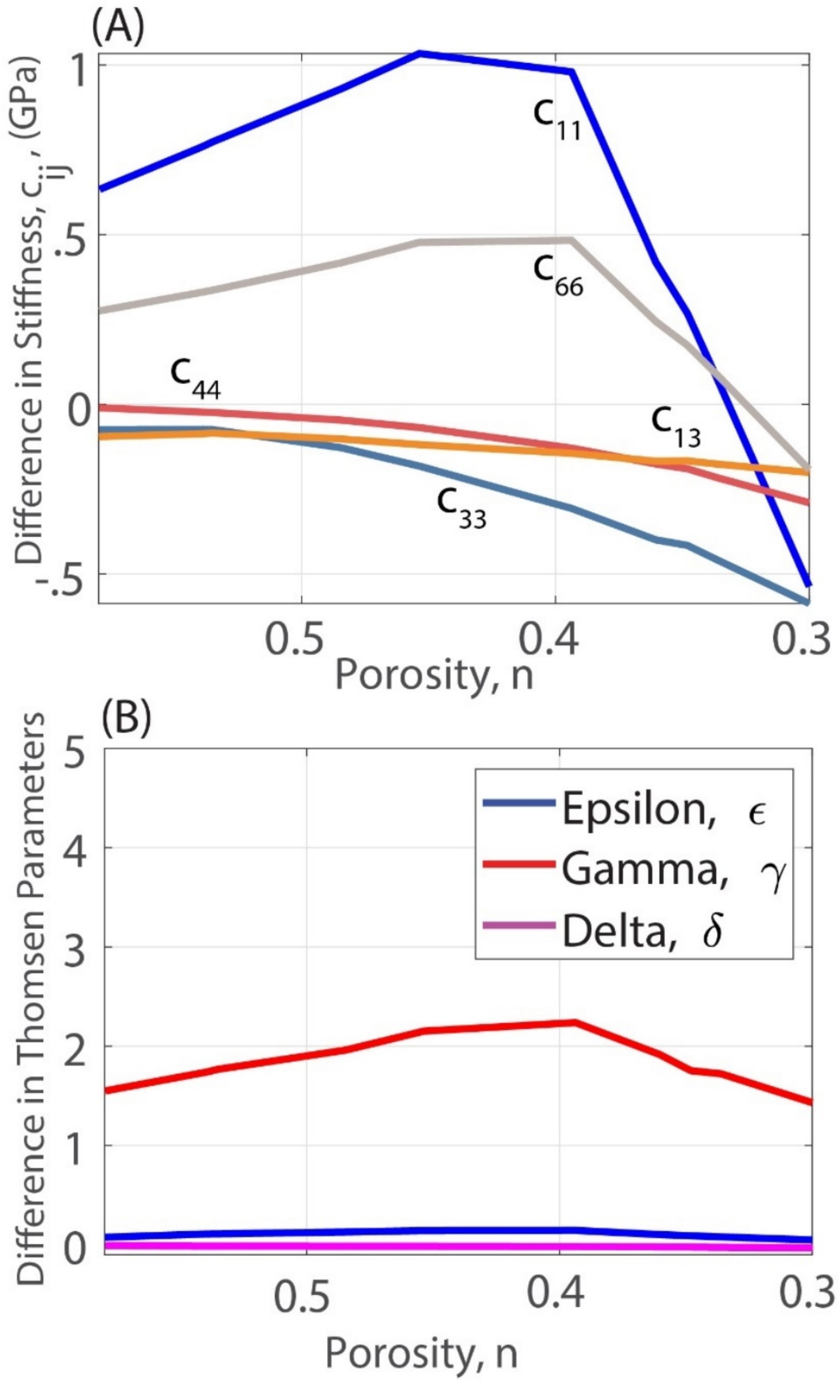


Figure 5: Difference in (A) elastic stiffness matrix and (B) Thomsen parameters of a building block for lithology of 65 % Clay and 35 % Quartz to 25% Clay and 75% Quartz vs porosity.

### 2.2.3 Determination of Building Block Alignments due to Deformation

I now describe the distribution of orientations of building blocks due to any strain. I first establish a local coordinate system for the building blocks $(x_1, x_2, x_3)$ and a global coordinate system aligned to the principal strain axes $(X_1, X_2, X_3)$. The orientation of any building block is described by the Euler angles (Figure 6C) $\theta$ (the angle between $x_1$ and the $X_1$ axes), $\psi$ (the rotation about the vertical, $X_1$, axis), and $\phi$ (rotation about the local, $x_1$, axis). The orientation distribution function (ODF) then is $W(\xi, \psi, \phi)$, where $\xi = cos\theta$ (Sayers, 1994).

March (1932) derived an expression that gives the directional distribution function (DDF) to describe the density of poles to the building blocks, *f*, as a function of strain (Figure 6B), assuming that the building blocks are initially randomly oriented (Figure 6A). Owens (1973) extended this model to include the effects of volume change and for any initial distribution. His general relationship is,

$$f_f(\xi, \psi) = \frac{1}{1 - \epsilon_{vol}} \left(\frac{D_f}{D_i}\right)^3 f_i(\xi, \psi)$$

$$= \frac{\left(D_{11f}^2 \xi^2 + D_{22f}^2 (1-\xi)^2 \sin^2 \psi + D_{22f}^2 (1-\xi)^2 \cos^2 \psi\right)^{\frac{3}{2}}}{D_{11f} D_{22f} D_{33f}} f_i(\xi, \psi). \tag{15}$$

*f* is the angular density of poles at $\xi = cos\theta$ and $\psi$, $D$ is the principal deformation matrix (Baker et al., 1993). The principal deformation matrix is,

$$D = \begin{bmatrix} D_{11} & 0 & 0 \\ 0 & D_{22} & 0 \\ 0 & 0 & D_{33} \end{bmatrix}, \tag{16}$$

where, the matrix defines the shape and orientation of the strain ellipsoid. The diagonals ($D_{11}$,$D_{22}$,$D_{33}$) describe the length of its principal axes (Fossen, 2016). $\epsilon_{vol}$, the volumetric deformation is equal to the difference between the initial and final multiplications of the principal deformation axes – $D_{11}*D_{22}*D_{33}$.

The expression derived by Owens (1973) is independent of $\phi$, the angle of rotation around the local z-axis of each individual domain. In order to use the DDF, $f$, as an ODF (equation 15) I introduce $\phi$ with the addition of a scaling factor of 2π (Johansen et al., 2004),

$$W(\xi,\psi,\phi) = \frac{1}{2\pi} f(\xi,\psi) = \frac{1}{2\pi}\frac{1}{1-\epsilon_{vol}}\left(\frac{D_f}{D_i}\right)^3 f_i(\xi,\psi)\ . \tag{17}$$

Equation 17 allows for the computation of the probability density of building blocks at all orientations (Figure 6B) with only the principal deformation tensor, initial distribution (Figure 6A), and corresponding volumetric deformation. The construction of Equation 17 is further detailed in appendix A.

The initial distribution is input into the calculation of the final alignment. Multiple theories have been proposed to explain the orientation of clay particles upon deposition. Three primary theories have gained popularity: 'Honeycomb' structure (Morris and Żbik, 2009; O'Brien, 1971), 'Cardhouse' structure (Van Olphen, 1964), and a randomly distributed structure (Deirieh et al., 2018). In my work, I use a random distribution of clay particles to represent the initially deposited clay particle alignment based on analysis of micro-scale images (Figure 1A, Figure 6C) (Adams et al., 2013) and experiments on frozen, high-pressure clay slurries (Deirieh et al., 2018).

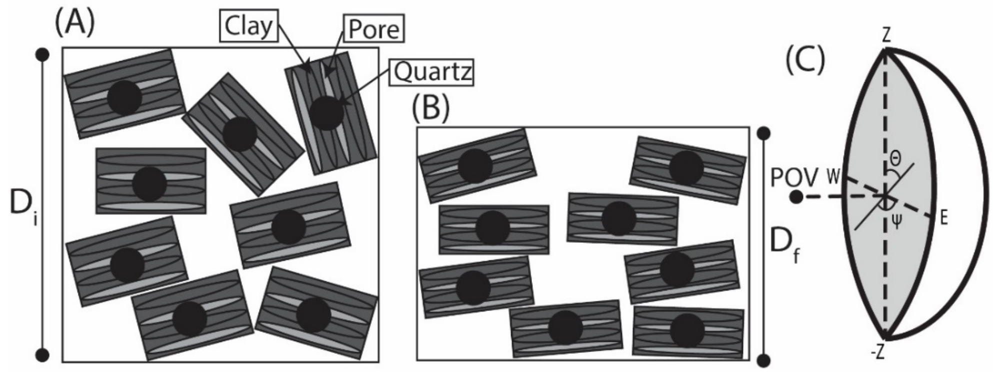


Figure 6: 2-D Cartoon depictions of a mudrock at (A) unstrained and (B) 33 % uniaxially strained conditions. Uniaxial compaction leads to porosity loss within the blocks (noted by the change in pore sizes) and the collapse of building blocks to preferential alignment perpendicular to the loading direction as seen in the changes between images A and B. Images are of a vertical plane parallel to the axial loading direction. The orientation of each building block relative to the principal strain axes is described through the Euler angles (C). (C) depicts point of view (POV) of stereogram.

### 2.2.4 Alignment due to Deformation

I use Equation 17 to describe the evolution of alignment under uniaxial strain and pure shear. To apply Equation 17, I need to determine the change in the principal deformation axes, volumetric strain, and initial distribution. Under uniaxial strain (Figure 7B), one principal strain axis undergoes contraction without any change in length along the other two (Fossen, 2016). This is described by a decrease in the principal deformation axis; $D_{11}$. $D_{22}$ and $D_{33}$ remain equal to one. The volumetric strain corresponds to the change in the final volume equal of $D_{11}*D_{22}*D_{33}$. The initial distribution, $f_i(\xi,\psi)$, is assumed to be random (Figure 7A) (Deirieh et al., 2018).

The alignment is described by plotting the poles to the building blocks in a stereogram (Figure 7B). These poles are perpendicular to the plane of the building block- Originally, the poles are randomly distributed and thus no contours are present (Figure 7A). However, after a distortion ratio of 40 %, there is considerable alignment with the density of poles clustered along the vertical in the stereogram increased (Figure 7B, Darker red). The distortion ratio is the ratio of the maximum principal deformation axis to the minimum principal deformation axis. In the case of uniaxial strain, the distortion is equivalent to the vertical strain. The poles to the building blocks show a mean of 0 degrees and standard deviation of $\pm$ 33.5 degrees to the vertical axis when fit with a normal distribution.

Under pure shear, there is an equal amount of shortening along one principal axis and extension along the other while the third axis remains constant (Fossen, 2016). To determine the final alignment from pure shear, I need to define the change in the principal deformation axes, the volumetric strain, and the initial distribution. The deformation leads to a shortening in the length of the principal deformation axes, $D_{11}$, while corresponding to an equal lengthening in $D_{22}$, while $D_{33}$ remains equal to one. The initial distribution is assumed to be random.

Under pure shear, the density of poles to building blocks increases aligned to the vertical (Figure 7C). The poles to the building blocks show a mean of 0 degrees and standard deviation of $\pm$ 45 degrees to the vertical axis when fit with a normal distribution. This means pure shear deformation leads to an increased density of building blocks perpendicular to the shortening direction.

There is an increase in alignment with increased distortion under both uniaxial strain and pure shear (Figure 7). However, for the same amount of distortion, there is a greater degree of alignment under uniaxial strain relative to pure shear shown by the smaller standard deviation in uniaxial strain (33.5 degrees) to pure shear (45 degrees) and increased density of poles clustered near the vertical (darker red contours). Conceptually, the volume of the element of mudrock decreases in the uniaxial strain case, whereas there is no volume change under pure shear. The platy particles are forced to align more due to the smaller volume they must fit into.

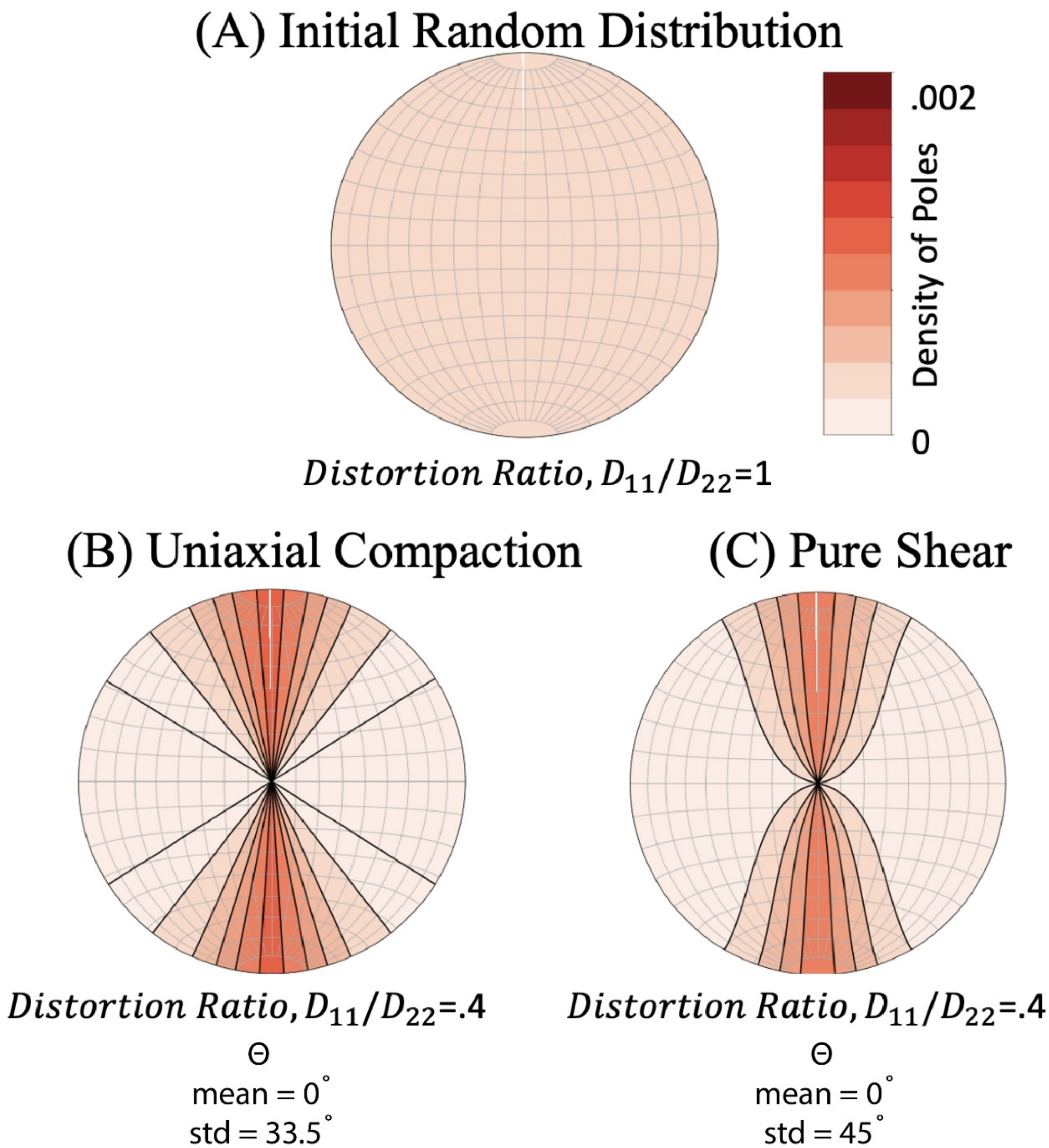


Figure 7: Stereograms of the density of poles to building blocks from (A) an initially random distribution, (B) uniaxial compaction, and (C) pure shear deformation. The standard deviation of alignment of poles away from the vertical are 33.5 degrees in uniaxial compaction vs 45 degrees in pure shear. Comparison of (B) and (C) shows a larger alignment due to uniaxial compaction versus pure shear deformation. Distortion ratio represents the ratio of the maximum principal deformation axis to the minimum principal deformation axis. Contours every .0002 increase in density.

### 2.2.5 Combination of Elastic Stiffnesses and Alignments

I obtain the final elastic stiffness matrix representative of a mudrock with a Voigt approximation over all orientations of building block effective elastic stiffnesses (Sayers, 1994). The function is evaluated by expanding the ODF, $W(\xi, \psi, \phi)$ into generalized spherical harmonics (Morris, 1969; Roe, 1965),

$$W(\xi, \psi, \phi) = \sum_{l=0}^{\infty} \sum_{m=-l}^{l} \sum_{k=-l}^{l} W_{lmk} Z_{lmk}(\xi) e^{-im\psi} e^{-ik\phi}, \tag{18}$$

where $Z_{lmk}(\xi)$ are generalized Legendre functions and $W_{lmk}$ are Legendre coefficients (Johansen et al., 2004). I use a limited number of Legendre coefficients, $W_{lmk}$, to combine the building block elastic stiffnesses and ODF. The limited number of coefficients represent the maximum possible amount of information obtainable for the ODF using elastic waves with wavelengths large compared to the particle size (Sayers, 2005). The only coefficients, $W_{lmk}$, of the expansion of $W(\xi, \psi, \phi)$ considered are for $l \leq 4$ because the elastic stiffness tensor is of fourth rank.

To apply equation 18 the components must be transversely isotropic (TI) and the orientation distribution must be orthotropic (Sayers, 1994) with symmetry axes aligned along the principal strain axes $(X_1, Y_1, Z_1)$. Orthotropic materials have material properties that differ along three orthogonal axes. The building block is constructed as a TI medium and the Owens-March function based on the principal deformation matrix results in an orthotropic distribution (Sayers, 1994). The nonzero $W_{lmk}$ are then all real and vanish unless *1* and *m* are even and $k = 0$ because my effective medium is orthotropic and building blocks are a TI medium (Sayers, 1994). The elastic stiffnesses are therefore determined in this case by five coefficients ($W_{200}, W_{220}, W_{400}, W_{420}, W_{440}$) (Sayers, 1994). Appendix 1 contains the equations to determine the orthotropic elastic stiffness matrix of the mechanically compacted mudrock based on the five Legendre coefficients and the building block elastic stiffness matrix from Sayers (1994).

In the case of a TI distribution of building blocks with symmetry axis along the principal axes, $X_1$, $W_{220} = W_{420} = W_{440} = 0$, then two expansion coefficients of the ODF determine the elastic stiffnesses ($W_{200}$ *and* $W_{400}$). If the building blocks have a completely random orientation, i.e., $W_{200} = W_{400} = 0$, the mudrock is an isotropic medium (Johansen et al., 2004; Sayers, 1994).

### 2.2.6 Mudrock Elastic Stiffnesses

Results for the cases of uniaxial compaction and pure shear deformation are displayed in Figures 8 and 9 (Uniaxial Compaction) and 10 and 11 (Pure Shear Deformation). In both cases I assume an initial porosity as .57 (Figure 1A) from low stress (.1 MPa) measurements and the lithology fractions (65% Clay and 35% Quartz) based on core measurements of Gulf of Mexico – Eugene Island (GOM-EI) (Ranjpour, 2020) and elastic properties for constituents from (Mavko et al., 2009) (Table 3).

Figure 8A shows the TI elastic stiffness matrix for a mudrock during uniaxial compaction (dashed lines) along with the elastic stiffness of an individual building block (solid lines) versus porosity. At the initial porosity of 0.57, the random distribution of building blocks creates isotropic elastic properties and effectively averages the building compressional and shear elastic properties (Figure 1A, 8A). Porosity reduction increases each elastic stiffness matrix value. The introduction of a distribution reduces the compressional and shear anisotropy at all porosities (Figure 8B)

Figure 9A shows the corresponding Thomsen (1986) parameters versus porosity. The initial isotropic distribution has Thomsen's parameters equal to zero (Figure 9A) due to the random distribution of building blocks. Seismic anisotropy increase as the mudrock undergoes uniaxial compaction, and the mudrock experiences porosity loss and domain alignment (Figure 1B, 8A). The elastic anisotropy of the mudrock is significantly reduced compared to a single building block due to the distribution of building blocks versus purely aligned ellipsoidal inclusions (Figure 9B).

In my second endmember—pure shear (Figure 10 and 11)— the mudrock again begins at isotropic conditions (dashed lines) compared to the initial anisotropic properties of the building block (solid lines). The magnitude of the average of the compressional ($c_{11}, c_{33}$) and shear ($c_{44}, c_{66}$) stiffnesses remains the same as the initial conditions because the initial porosity of 0.57 is maintained throughout deformation. However, pure shear deformation aligns building blocks, and as a result elastic anisotropy develops (Figure 11A). The introduction of an aligned distribution of building blocks reduces the difference between the mudrock and building block elastic stiffnesses with increased distortion (Figure 10B).

Finally, I compare the variation of elastic properties with porosity predicted by my workflow (Figure 12) to experimental results of mudrocks undergoing uniaxial compaction (Ranjpour, 2020) (Open circles; Figure 12) (Nihei et al., 2011) (Closed circles; Figure 12). The modeled results match results shown in Figure 8 and 9. These properties include bulk rock fractions from Gulf of Mexico – Eugene Island Samples (GOM-EI) (Ranjpour, 2020), 65% Clay and 35% Quartz, and elastic properties from Mavko et al. (2009) (Table 2). The samples from Nihei et al. (2011) are intact samples with a similar lithology to the GOM-EI samples (Ranjpour, 2020). The modeled compressional elastic stiffnesses match experimental data within 10% (Figure 12; Data points plot within 10% of $c_{11}$ and $c_{33}$). The results fail to properly match the shear elastic stiffnesses within 10 % error (Figure 12; Data points fail to fall within 10% of $c_{44}$ and $c_{66}$).

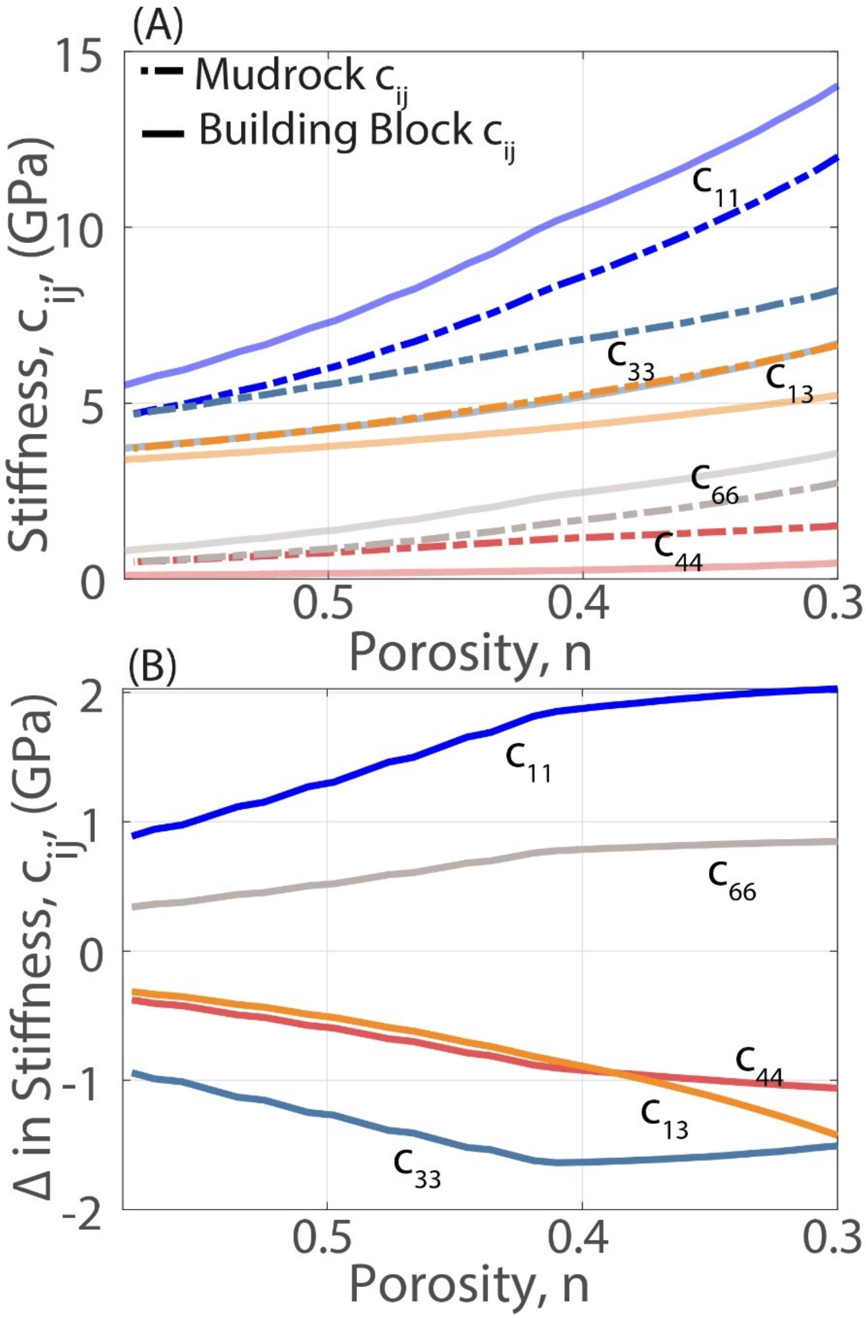


Figure 8: (A) Comparison of Building Block (Solid Lines) and mudrock undergoing uniaxial strain (dashed lines) TI elastic stiffness matrix and (B) change in elastic stiffnesses between building block and mudrock vs porosity. The bulk rock composition is 65% clay and 35% quartz.

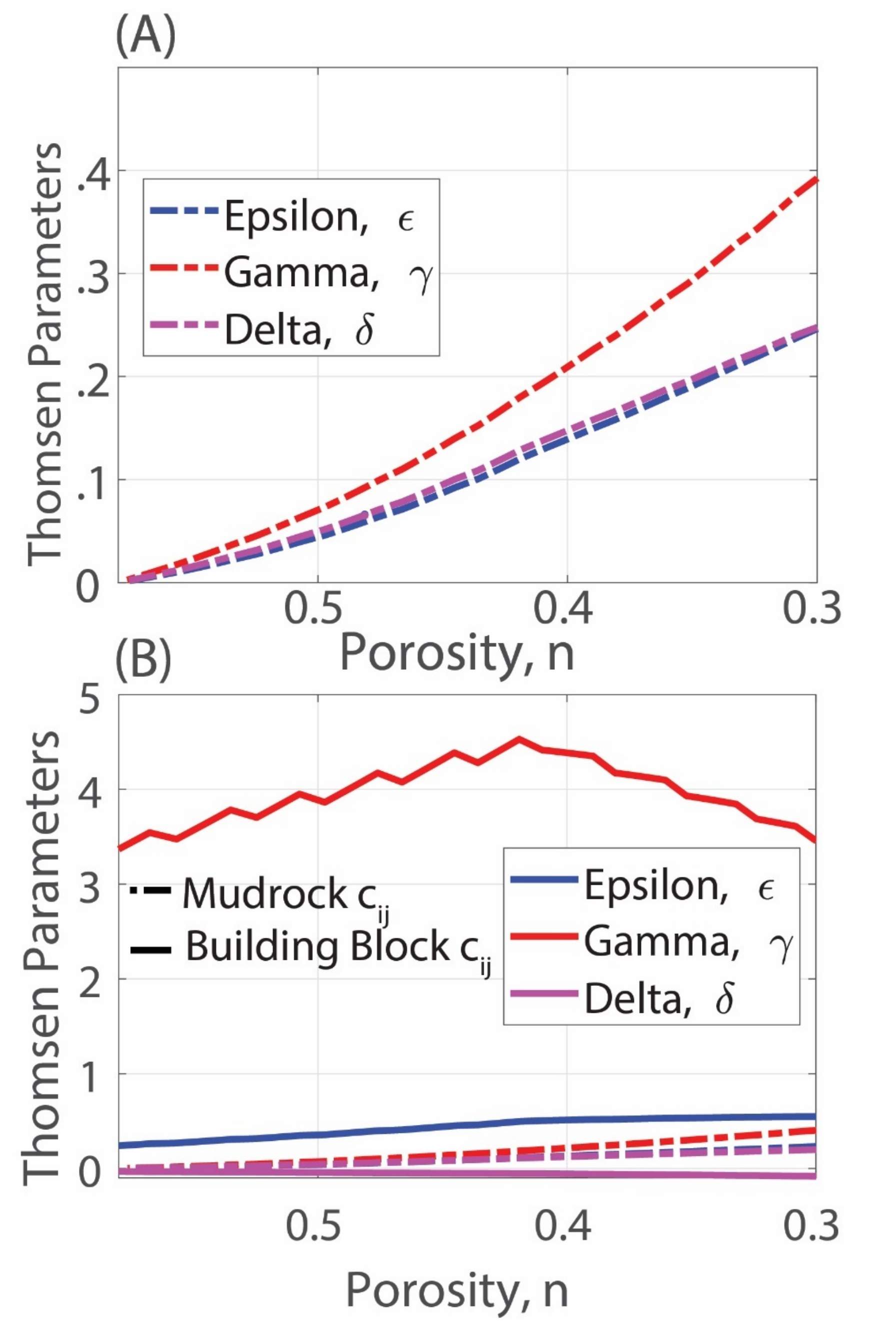


Figure 9: (A) Thomsen' parameters of a mudrock undergoing uniaxial strain (dashed lines) and (B) Thomsen' parameters of a mudrock undergoing uniaxial strain (dashed lines) and building block (solid lines) vs porosity. Note change in y axis scale between (A) and (B). The bulk rock composition is 65% clay and 35% quartz.

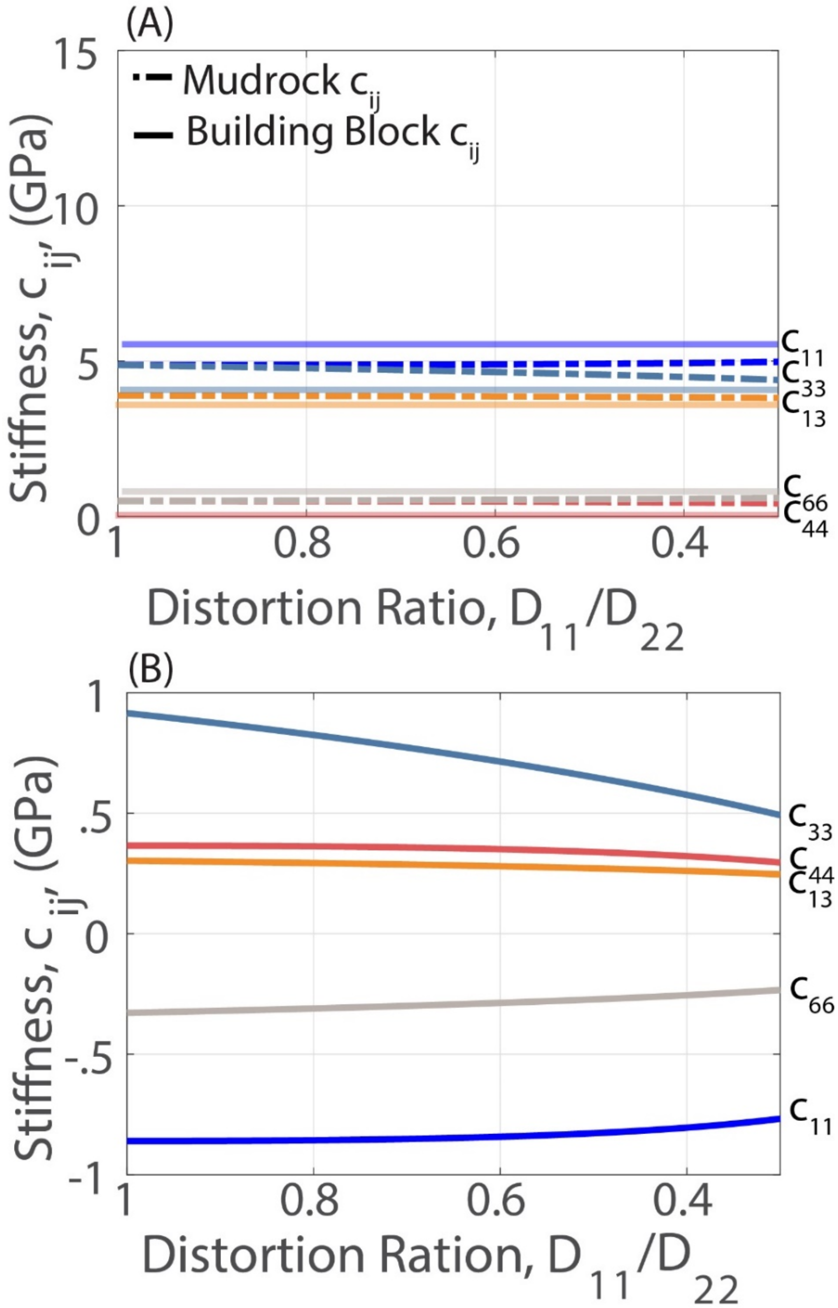


Figure 10: (A) Comparison of Building Block (Solid Lines) and mudrock undergoing pure shear deformation (dashed lines) TI elastic stiffness matrix and (B) change in elastic stiffnesses between building block and mudrock vs porosity. The bulk rock composition is 65% clay and 35% quartz.

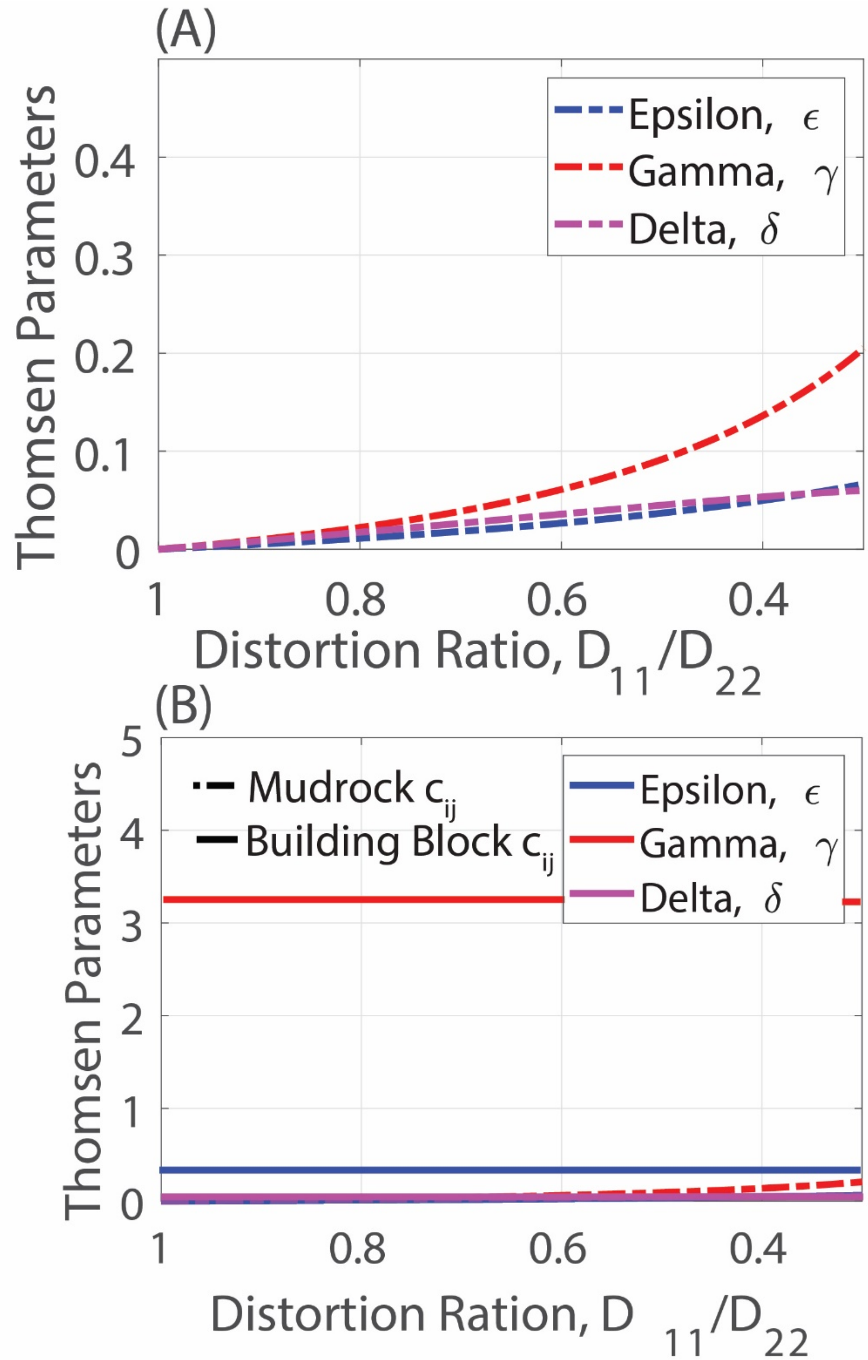


Figure 11: (A) Thomsen' parameters of a mudrock undergoing pure shear (dashed lines) and (B) Thomsen' parameters of a mudrock undergoing pure shear (dashed lines) and building block (solid lines) vs porosity. Note change in y axis scale between (A) and (B). The bulk rock composition is 65% clay and 35% quartz.

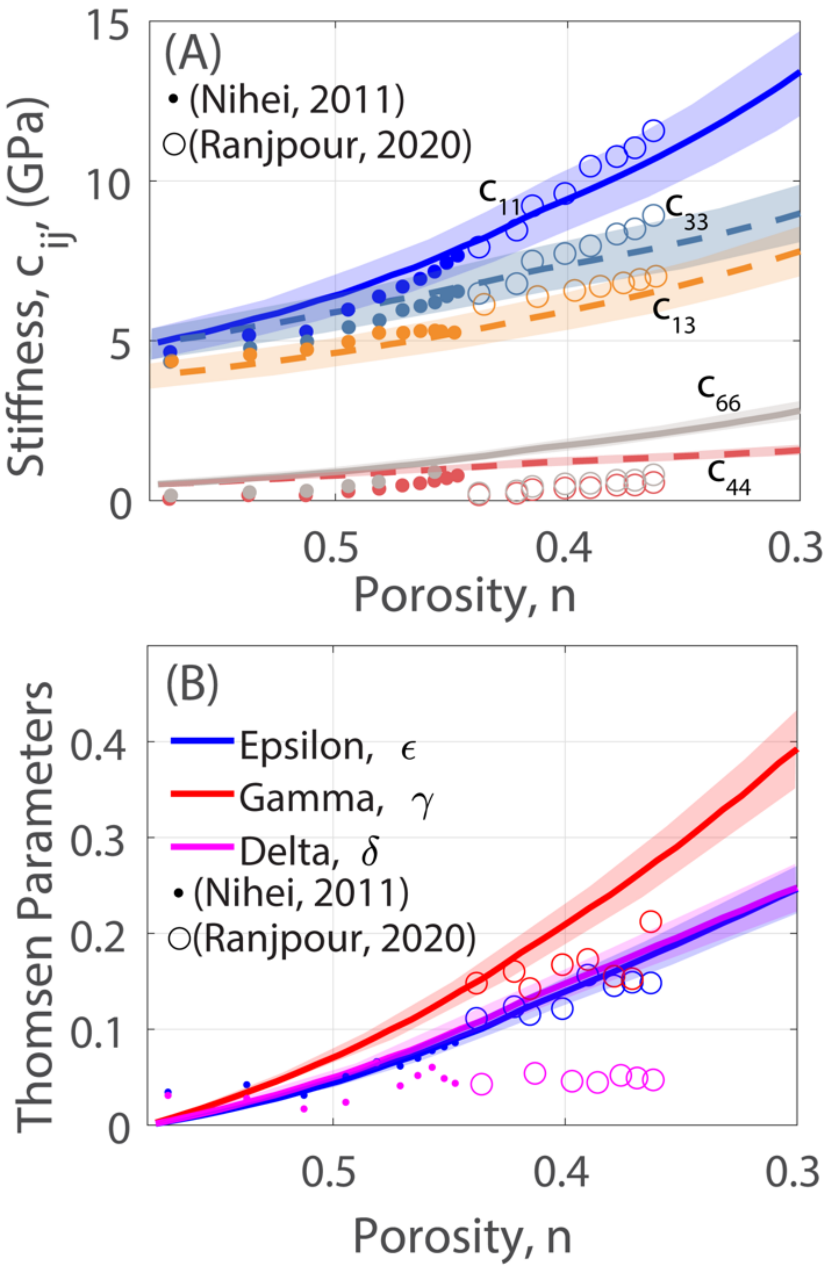


Figure 12: Prediction of (A) TI elastic stiffness matrix and (B) Thomsen' parameters for a mudrock undergoing uniaxial compaction vs porosity. The bulk rock composition is 65% clay and 35% quartz. Modeled results match Figure 9 and 10. Previously modeled results are overlain by experimental data from Nihei et al. (2011) and Ranjpour (2020). Shading represents 10% error of the model results.

### 2.2.7 Case Study

The workflow described holds several practical applications. Here I combine the workflow with a poromechanical model to investigate the impact of the full strain tensor on elastic stiffnesses. I apply my workflow to the outputs of the full strain tensor and porosity from a poromechanical model of a salt diapir rising through sediment (Nikolinakou et al., 2016) to predict elastic stiffnesses in the synthetic basin.

The evolutionary poromechanical model starts with an initially flat layer of salt which is then incrementally loaded with sediment. The salt upbuilds to the basin surface along the left edge of the modeled cross section (Figure 13). The final porosity distribution (Figure 13A) and deformation tensor components (overlying crosses) result from burial as well as loading from the growing salt diapir. The overlying crosses located at selected elements across the basin (Figure 13A) represent the maximum, $D_{11}$(blue), and minimum, $D_{33}$(black), principal deformation axes and are initially equal in length and oriented vertical/horizontal. Subsequent deformation is illustrated by the rotation and relative magnitude change of the two axes.

Two areas within Figure 13A illustrate examples of deformation. First, away from salt, both axes shorten with depth. This records the large reduction in porosity (color contours). Below the salt sheet, the maximum deformation axis rotates to be perpendicular to the salt-sediment interface. There is significant shortening in the direction normal to salt, and significant extension in the direction parallel to salt. As a result, porosity remains high despite the increase in overburden.

I use the deformation tensor at each element at the end of the simulation as input to my model. Other inputs for the effective medium model follow the properties defined earlier in the workflow (Table 2). These properties include bulk rock fractions from Gulf of Mexico – Eugene Island Samples (GOM-EI) (Ranjpour, 2020), 65% Clay and 35% Quartz, and elastic properties from Mavko et al. (2009) (Table 2).

With these inputs, I calculate the elastic stiffnesses at each location in the modeled cross section (Figure 13B). The angle defining the axis of symmetry for the TTI matrix is equal to the angle from the horizontal to the orientation of the minimum deformation axis. $\epsilon$ (equation 15) represents the fractional difference between the horizontal and vertical elastic stiffnesses (Thomsen, 1986). The overlying crosses show the maximum, $c_{11}$, and minimum, $c_{33}$, elastic stiffnesses.

Examining the same two areas in Figure 13B as 13A I see three key details. First along the right side of the image, where large porosity reduction occurred, both elastic stiffnesses greatly increase in magnitude and very little anisotropy is introduced. The equal shortening of both axes increased the elastic stiffnesses, but with no distortion of the axes lengths there is no introduction of anisotropy. Second, in proximity to salt higher values of anisotropy are introduced with a large difference between the two compressional elastic stiffness and the axis of symmetry of the elastic stiffness matrix rotates significantly.

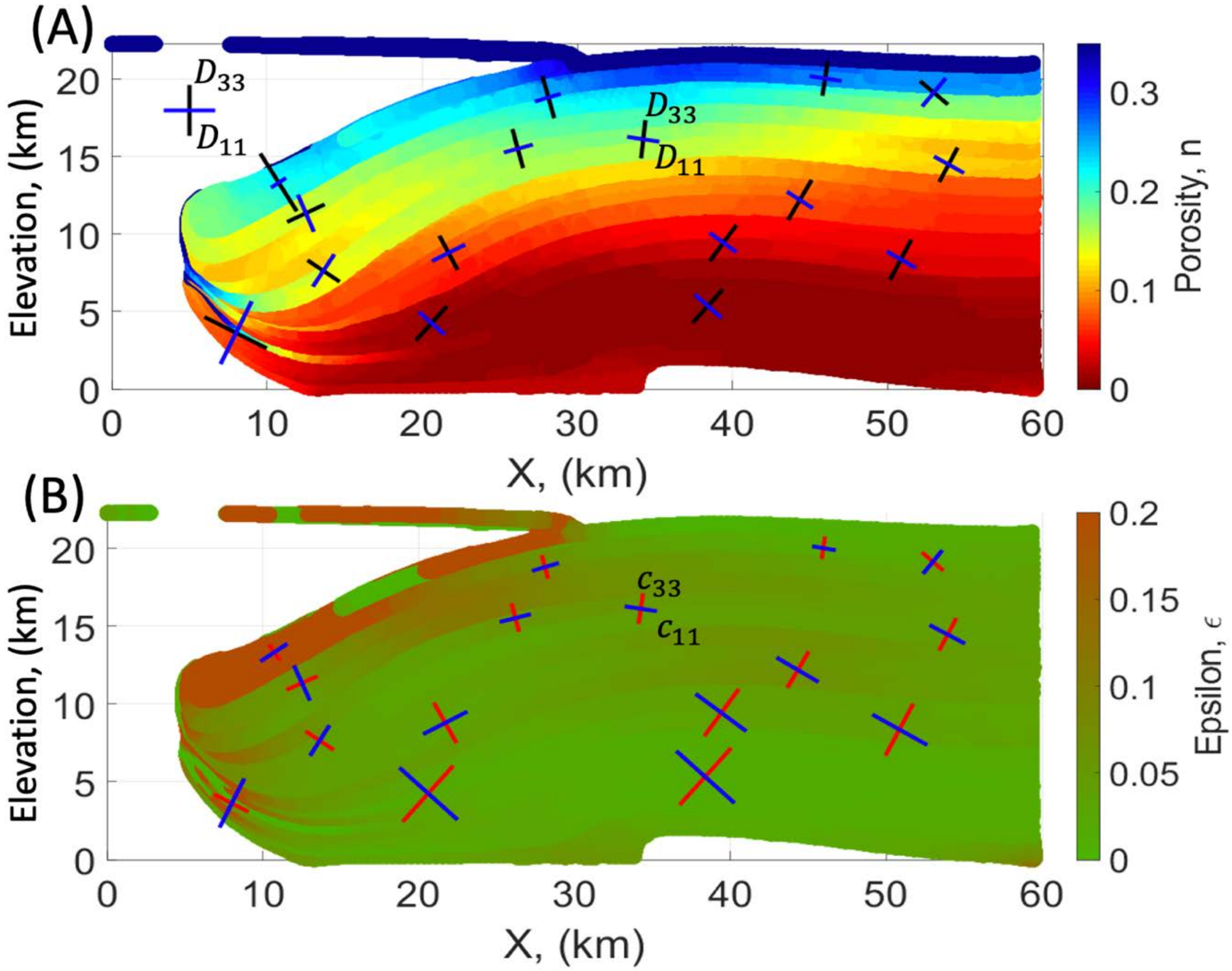


Figure 13: Cross-Section of the last time step of a poromechanical model of sediment deformed by deposition and a rising salt diapir. In (A), color contours represent porosity; bars illustrate the orientation and relative magnitude of the maximum, $D_{11}$(blue), and minimum, $D_{33}$(black), principal deformation axes. In (B), color contours represent the Thomsen' parameter epsilon, $\epsilon$; bars illustrate the orientation and relative magnitude of the maximum, $c_{11}$, (blue) and minimum, $c_{33}$, (red) in-plane elastic stiffnesses.

### 2.3 Discussion

The scientific contribution of this work is two-fold: (1) I successfully modeled the impact of deformation on elastic stiffnesses and (2) I illustrated two key sources of seismic anisotropy in compacted mudrocks: porosity reduction and grain reorientation. The anisotropy introduced through porosity reduction is seen in the modeling of building blocks (Figure 3 and 4). The elastic anisotropy introduced by grain alignment is seen in the modeling of the entire mudrock (Figure 9 and 11). My workflow provides a novel method for the prediction of the elastic stiffness matrix from any strain tensor and constituent properties (fractions and elastic properties).

Porosity reduction and building block reorientation separately impact the mudrock elastic stiffnesses. The overall magnitude of the building block elastic stiffnesses and seismic anisotropy increase with porosity reduction (Figure 3 and 4). The lithology of the building lock has very little impact on the elastic stiffness matrix but does impact the level of shear anisotropy (Figure 3 – 65% Clay and 35% Quartz vs Figure 4 25% Clay and 75% Quartz). The high shear anisotropy in the building blocks is due to $c_{44}$, the minimum shear stiffness, which approaches zero because of the thin ellipsoidal shape of the clay grains vs the circular shape of quartz grains. The introduction of misaligned building blocks lowers the shear anisotropy to a more reasonable level.

Increased alignment of building blocks without porosity reduction increases the elastic anisotropy of the mudrock but has no impact on the magnitude of the average of the compressional ($c_{11}, c_{33}$) and shear ($c_{44}, c_{66}$) stiffnesses (Pure shear; Figure 10 and

11). Uniaxial compaction shows the increase in elastic stiffnesses and anisotropy from the combined impact of porosity reduction and building block alignment (Figure 8 and 9).

Ultimately the model must be compared to experimental results to demonstrate its usefulness. Uniaxial compaction laboratory measurements on mudrocks show increasing elastic stiffnesses and the development of seismic anisotropy at higher stresses (Figure 12). I interpret these characteristics to be due to both the alignment of domains and the decline in porosity. The modeled compressional elastic stiffnesses match experimental data within 10 %. However, the error in predicting the shear elastic stiffnesses is larger than 10 %. A possible reason for this discrepancy is the March (1932) model overpredicts the reorientation of grains leading to higher shear elastic stiffnesses with greater alignment. Nonetheless, my results generate a close prediction to both the magnitude of compressional elastic stiffnesses (Figure 11) and values of $\epsilon$, compressional elastic anisotropy (Figure 11).

The elastic properties assumed for clay minerals are highly uncertain due to an inability to measure individual clay crystals (Katahara, 1996). I assumed the constituent elastic properties for quartz and clay from Han et al. (1986) due to the similarity in lithology to our core measurements. Any change in the clay elastic properties impacts the building block elastic properties and final results. I also assumed that pores and clay aggregates can be described as ellipsoidal inclusions with a length to width ratio of 10 to 1. The aspect ratio will impact the degree of anisotropy.

Further, I assumed that domains of locally aligned clay and pore are approximated as aligned thin ellipsoidal inclusions. In fact, these domains do not appear to be perfectly aligned (e.g., Figure 1). Finally, the re-orientation of domains is approximated by a linear or planar element that behaves as a passive, geometrical element (Owens, 1973). It is possible that at small strains, grains get locked into their positions and the March model overpredicts further reorientation (Adams et al., 2013). In my work, these assumptions create a simplified model of a mudrock, which, admittedly, sacrifices some aspects of accuracy but allows for the direct examination of the impact of deformation on elastic stiffnesses and anisotropy.

In the case study I predict the elastic stiffness matrix of mudrocks based on the full strain tensor through the combination of my workflow with a poromechanical model. This example clearly shows that anisotropy is not a simple function of depth or bedding orientation. The results illustrate the increase of elastic stiffnesses in areas of large porosity reduction from compaction. Additionally, I observe that sediment in close proximity to salt undergoes almost pure shear deformation with a rotation of the principal strain axes toward perpendicular to salt. This results in increased values of compressional anisotropy, with large differences between the maximum, $c_{11}$, and minimum, $c_{33}$, compressional elastic stiffnesses and a rotation of the axis of symmetry (Figure 13B). My work provides a framework to estimate the TTI elastic stiffness matrix as a function of the stress state and cumulative deformation undergone by a mudrock.

In addition to the combination with a poromechanical model, two additional potential applications include: 1) The prediction of a TTI elastic stiffness matrix from stress and associated strain models could be combined with seismic processing methods to improve imaging in areas of complex deformation. 2) The workflow could be used with inverted elastic stiffnesses to extract stress state and deformation information along with the axis of symmetry from field data. In conventional seismic processing of anisotropic media, the axis of symmetry is oriented either vertically (TI) or perpendicular to dip (TTI). My approach considers the rotation of the axis of symmetry due to angle of the principal strain tensor. These considerations provide the potential to improve seismic imaging in highly deformed geologic environments.

## 2.4 CONCLUSIONS

I have introduced a novel workflow to compute the full elastic stiffness matrix of a mechanically compacted mudrock based on its full strain tensor. The elastic stiffness matrix is modeled in three primary steps. (1) I initially compute an effective medium model representative of locally aligned clay particles and pores ('a domain') with isolated isotropic quartz grains. The combined SCA/DEM formulation creates the building block for the computation of the bulk mudrock elastic stiffnesses. (2) I predict the alignment of multiple building blocks due to any strain case through the Owens-March ODF. (3) The single building block effective elastic stiffness matrix and ODF are combined to compute an effective elastic stiffness matrix representative of a mechanically compacted mudrock which has undergone any deformation.

My model allows for the prediction of the full elastic stiffness matrix and seismic anisotropy for a mudrock based on the full strain tensor and constituent properties (fractions and elastic properties). The compressional results from my forward model strongly correlate with the experimental data seen in both Nihei et al. (2011) and

Ranjpour (2020). I constrain two key relationships between deformation and elastic stiffnesses. First, porosity loss increases the overall magnitudes of the entire matrix and seismic anisotropy. Second, building block alignment leads to significant increases in elastic anisotropy.

The workflow outlined has multiple practical applications including the integration with poromechanical model outputs highlighted in the case study. The combination allows for investigation of the impact of complex strains on mudrock elastic properties. The workflow has two more potential applications. first, the elastic stiffness matrix and principal angle may be combined with TTI seismic processing to improve imaging of the subsurface. Second, it can be used with inverse methods to examine deformation from field data based on inverted elastic stiffnesses. Overall, I produce a workflow to estimate the elastic stiffness matrix of mudrock based on the full strain tensor which matches experimental data.

## 2.5 Appendix 1: Full Elastic Stiffness Matrix Calculation

The elastic stiffnesses are computed from all non-zero Legendre coefficients ($W_{200}, W_{220}, W_{400}, W_{420}$ and $W_{440}$) and the three anisotropy factors $a_1, a_2$, and $a_3$ defined below. I assume the building block elastic stiffness matrix is transverse isotropic (TI) and the mudrock exhibits orthotropic symmetry (Sayers, 1994). In Sayers (1994) the equations to describe effective elastic stiffnesses from aligned elastic stiffnesses and an ODF are formulated as follows:

$$c_{11} = \lambda + 2\mu + \frac{8\sqrt{10}}{105}\pi^2 a_3\left(W_{200} - \sqrt{6}W_{220}\right) + \frac{4\sqrt{2}}{35}\pi^2 a_1\left(W_{400} - \frac{2\sqrt{10}}{3}W_{420} + \frac{\sqrt{70}}{3}W_{440}\right), \quad (19)$$

$$c_{22} = \lambda + 2\mu + \frac{8\sqrt{10}}{105}\pi^2 a_3\left(W_{200} + \sqrt{6}W_{220}\right) + \frac{4\sqrt{2}}{35}\pi^2 a_1\left(W_{400} + \frac{2\sqrt{10}}{3}W_{420} + \frac{\sqrt{70}}{3}W_{440}\right), \quad (20)$$

$$c_{33} = \lambda + 2\mu - \frac{16\sqrt{2}}{105}\pi^2\left(\sqrt{5}a_3 W_{200} - 2a_1 W_{400}\right), \quad (21)$$

$$c_{12} = \lambda - \frac{8\sqrt{10}}{315}\pi^2(7a_2 - a_3)W_{200} + \frac{4\sqrt{2}}{105}\pi^2 a_1\left(W_{400} - \sqrt{70}W_{440}\right), \quad (22)$$

$$c_{13} = \lambda + \frac{4\sqrt{10}}{315}\pi^2(7a_2 - a_3)\left(W_{200} + \sqrt{6}W_{220}\right) - \frac{16\sqrt{2}}{105}\pi^2 a_1\left(W_{400} - \sqrt{\frac{5}{2}}W_{420}\right), \quad (23)$$

$$c_{23} = \lambda + \frac{4\sqrt{10}}{315}\pi^2(7a_2 - a_3)\left(W_{200} - \sqrt{6}W_{220}\right) - \frac{16\sqrt{2}}{105}\pi^2 a_1\left(W_{400} + \sqrt{\frac{5}{2}}W_{420}\right), \quad (24)$$

$$c_{44} = \mu - \frac{2\sqrt{10}}{315}\pi^2(7a_2 + 2a_3)\left(W_{200} - \sqrt{6}W_{220}\right) - \frac{16\sqrt{2}}{105}\pi^2 a_1\left(W_{400} + \sqrt{\frac{5}{2}}W_{420}\right), \quad (25)$$

$$c_{55} = \mu - \frac{2\sqrt{10}}{315}\pi^2(7a_2 + 2a_3)\left(W_{200} + \sqrt{6}W_{220}\right) - \frac{16\sqrt{2}}{105}\pi^2 a_1\left(W_{400} - \sqrt{\frac{5}{2}}W_{420}\right), (26)$$

$$c_{66} = \mu + \frac{4\sqrt{10}}{315}\pi^2(7a_2 + 2a_3)W_{200} + \frac{4\sqrt{2}}{105}\pi^2 a_1\left(W_{400} - \sqrt{70}W_{440}\right). \quad (27)$$

Where $\lambda\ and\ \mu$ are given by:

$$15\lambda = c_{11}^{dem} + c_{33}^{dem} + 5c_{12}^{dem} + 8c_{13}^{dem} - 4c_{44}^{dem}, \quad (28)$$

&

$$30\mu = 7c_{11}^{dem} + 2c_{33}^{dem} - 5c_{12}^{dem} - 4c_{13}^{dem} + 12c_{44}^{dem}, \quad (29)$$

and $a_1, a_2, a_3$ are given by:

$$a_1 = c_{11}^{dem} + c_{33}^{dem} - 2c_{13}^{dem} - 4c_{44}^{dem}, \quad (30)$$

$$a_2 = c_{11}^{dem} - 3c_{12}^{dem} + 2c_{13}^{dem} - 2c_{44}^{dem}, \quad (31)$$

$$a_3 = 4c_{11}^{dem} - 3c_{33}^{dem} - c_{13}^{dem} - 2c_{44}^{dem}. \quad (32)$$

$$G = 1/8\pi[\bar{G}_{ijkl} + \bar{G}_{jkil}], \quad (33)$$

## 2.6 APPENDIX 2: SOLUTION OF G

G is a fourth rank tensor calculated from the response of an unbounded matrix of the effective medium (Bandyopadhyay, 2009). I initially set each matrix value of $c_{sca}$ to the average of the corresponding clay and fluid-filled porosity values and compute G. The inputs to solve for G are the estimated $c_{sca}$ and the chosen aspect ratio of the spheroidal inclusion, $\gamma$ (equation 52). For my model I set the aspect ratio, $\gamma$, to be 1/10. The procedure is repeated until $c_{sca}$ converges to a fixed value.

$$G_{ijkl} = \frac{1}{8\pi}[\bar{G}_{ijkl} + \bar{G}_{jkil}], \tag{34}$$

where,

$$\bar{G}_{ijkl} = (\alpha_1\alpha_2\alpha_3)\int_S N_{ij}(\xi)D^{-1}\xi\xi_l\xi_k\varsigma^{-3}dS(\xi), \tag{35}$$

$$\varsigma = (\alpha_1^2\xi_1^2 + \alpha_2^2\xi_2^2 + \alpha_3^2\xi_3^2)^{1/2}, \tag{36}$$

$$D(\xi) = \det(C_{ijkl}\xi_j\xi_l), \tag{37}$$

$$N_{ij} = cofactor(c_{ijkl}\xi_j\xi_l). \tag{38}$$

*S* is the unit sphere, $\xi$ is the unit vector forming *S*, and *ds* is the differential of the surface area on the unit sphere, and $\alpha_1, \alpha_2, \alpha_3$ are the three principal half axes of the ellipsoidal inclusion.

If the axes of the effective medium coincide with the principal axes of a spheroidal inclusion,

$$\frac{x_1^2}{\alpha_1^2} + \frac{x_2^2}{\alpha_2^2} + \frac{x_3^2}{\alpha_3^2} \leq 1, \tag{39}$$

and the non-zero coefficients of the $G_{ijkl}$ matrix are,

$$\bar{G}_{1111} = \bar{G}_{2222} = \frac{\pi}{2}\int_0^1 \Delta(1-x^2)\big([f(1-x^2) + h\gamma^2x^2][(3e+d)(1-x^2) + 4f\gamma^2x^2] - g^2\gamma^2x^2(1-x^2)\big)dx, \tag{40}$$

$$\bar{G}_{3333} = 4\pi\int_0^1 \Delta\gamma^2x^2[d(1-x^2) + f\gamma^2x^2][e(1-x^2) + f\gamma^2x^2]dx, \tag{41}$$

$$\bar{G}_{1122} = \bar{G}_{2211} = \frac{\pi}{2}\int_0^1 \Delta(1-x^2)\big([f(1-x^2)+h\gamma^2x^2][(e+3d)(1-x^2)+4f\gamma^2x^2]-3g^2\gamma^2x^2(1-x^2)\big)dx, \tag{42}$$

$$\bar{G}_{1133} = \bar{G}_{2233} = 2\pi\int_0^1 \Delta\gamma^2x^2\big([(d+e)(1-x^2)+2f\gamma^2x^2]*[f(1-x^2)+h\gamma^2x^2]-g^2\gamma^2x^2(1-x^2)\big)dx, \tag{43}$$

$$\bar{G}_{3311} = \bar{G}_{3322} = 2\pi\int_0^1 \Delta(1-x^2)[d(1-x^2)+f\gamma^2x^2][e(1-x^2)+f\gamma^2x^2]dx \tag{44}$$

$$\bar{G}_{1122} = \frac{\pi}{2}\int_0^1 \Delta(1-x^2)^2\big[g^2\gamma^2x^2-(d-e)[f(1-x^2)+h\gamma^2x^2]\big]dx, \tag{45}$$

$$\bar{G}_{1313} = \bar{G}_{2323} = -2\pi\int_0^1 \Delta g\gamma^2x^2(1-x^2)[e(1-x^2)+f\gamma^2x^2]dx, \tag{46}$$

where

$$\Delta^{-1} = [e(1-x^2)+f\gamma^2x^2]([d(1-x^2)+f\gamma^2x^2][f(1-x^2)+h\gamma^2x^2]-g^2\gamma^2x^2(1-x^2)), \tag{47}$$

$$d = c_{11} \tag{48}$$

$$e = (c_{11}-c_{12})/2 \tag{49}$$

$$f = c_{44} \tag{50}$$

$$g = c_{13}+c_{44} \tag{51}$$

$$h = c_{33} \tag{52}$$

$$\gamma = \frac{\alpha_1}{\alpha_3} \tag{53}$$

The fourth rank tensor, $\bar{G}_{ijkl}$, is represented in two-index notation as,

$$G_{ij} = \begin{bmatrix} G_{1111} & G_{1122} & G_{1133} & 0 & 0 & 0 \\ G_{1122} & G_{2222} & G_{1133} & 0 & 0 & 0 \\ G_{3311} & G_{3311} & G_{3333} & 0 & 0 & 0 \\ 0 & 0 & 0 & 2G_{1313} & 0 & 0 \\ 0 & 0 & 0 & 0 & 2G_{1313} & 0 \\ 0 & 0 & 0 & 0 & 0 & 2G_{1212} \end{bmatrix} \quad (54)$$

| Symbol | Name | Dimensions |
|---|---|---|
| $\mathbf{c_{ij}}$ | Elastic Stiffness Matrix | $M/(LT^2)$ |
| $\mathbf{c_{clay}}$ | Clay Elastic Stiffness Matrix | $M/(LT^2)$ |
| $\mathbf{c_{fluid}}$ | Fluid Elastic Stiffness Matrix | $M/(LT^2)$ |
| $\mathbf{c_{quartz}}$ | Quartz Elastic Stiffness Matrix | $M/(LT^2)$ |
| $\mathbf{c_{sca}}$ | Self-Consistent Approximation Elastic Stiffness Matrix | $M/(LT^2)$ |
| $\mathbf{c_{dem}}$ | Differential Effective Medium Elastic Stiffness Matrix | $M/(LT^2)$ |
| $\mathbf{n}$ | Porosity | Dimensionless |
| $\mathbf{n_{sca}}$ | Self-Consistent Matrix Porosity | Dimensionless |
| $\mathbf{n_{dem}}$ | Differential Effective Medium Porosity | Dimensionless |
| $\mathbf{n_{buildingblock}}$ | Final Building Block Porosity | Dimensionless |
| $\mathbf{v_{clayadd}}$ | Volume of clay replacing host medium | $L^3$ |
| $\mathbf{v_{fluidadd}}$ | Volume of fluid-filled porosity replacing host medium | $L^3$ |
| $\mathbf{v_{quartzadd}}$ | Volume of quartz replacing host medium | $L^3$ |
| $\boldsymbol{v}$ | Volume Concentration | $L^3$ |
| $\mathbf{f}$ | Angular Density Function | Dimensionless |
| $\mathbf{D_{ij}}$ | Deformation Matrix | L |
| $\mathbf{f}$ | Directional Distribution Function | Dimensionless |
| $\mathbf{W}$ | Orientation Distribution Function | Dimensionless |
| $\mathbf{x_1, x_2, x_3}$ | Building Block Axes | Dimensionless |
| $\mathbf{X_1, X_2, X_3}$ | Principal Strain Axes | Dimensionless |
| $\mathbf{Z_{lmk}}$ | Generalized Legendre Function | Dimensionless |
| $\mathbf{Q_{clay}}$ | Clay Inclusion Shape Factor | $M/(LT^2)$ |
| $\mathbf{Q_{fluid}}$ | Fluid Shape Inclusion Factor | $M/(LT^2)$ |
| $\mathbf{Q_{quartz}}$ | Quartz Shape Inclusion Factor | $M/(LT^2)$ |
| $\mathbf{G}$ | Geometric Strain Concentration factors | Dimensionless |
| $\mathbf{I}$ | Identity Matrix | $M/(LT^2)$ |
| $\mathbf{l, m}$ | Degree, Order | Dimensionless |
| $\mathbf{S}$ | Unit Sphere | Dimensionless |

Table 1. Nomenclature. *M = mass, L = length, and T = time.

| Symbol | Name | Dimensions |
|---|---|---|
| $\epsilon$ | Compressional Anisotropy | Dimensionless |
| $\gamma$ | Shear Anisotropy | Dimensionless |
| $\delta$ | Short Offset Anisotropy | Dimensionless |
| $\xi, \psi, \phi$ | Euler Angles | L/L |
| $\lambda$ | Lame's first parameter | $M/(LT^2)$ |
| $\mu$ | Lame's second parameter / Shear Modulus | $M/(LT^2)$ |
| $\mathrm{K}$ | Bulk Modulus | $M/(LT^2)$ |
| $\rho$ | Bulk Density | $M/L^3$ |
| $\xi$ | Unit Vector Forming S | Length |
| $\alpha_1, \alpha_2, \alpha_3$ | three principal half axes of the ellipsoidal inclusion | Length |
| $\epsilon_{vol}$ | Volumetric Strain | Dimensionless |

Table 2. Greek Letters Nomenclature. *M = mass, L = length, and T = time.

| | Quartz | Clay | Brine |
|---|---|---|---|
| $K\ (GPa)$ | **36** | **21** | **2.2** |
| $\mu\ (GPa)$ | **45** | **7** | **0** |
| $\rho\ (g/cm^3)$ | **2.65** | **2.85** | **1.05** |
| $v$ | **(1-*n*)*.35** | **(1-*n*)*.65** | ***n*** |

Table 3. Constituent Properties. Moduli based on Mavko et al. (2009) and volume concentration of each constituent match experimental sample of Gulf of Mexico – Eugene Island (GOM-EI) (Ranjpour, 2020).

# CHAPTER 3: APPENDICES

## Appendix A. Derivation of March-Owens Orientation Distribution Function

This appendix summarized the derivation of the Owens-March Orientation Distribution Function to describe the alignment of grains due to any deformation case. March (1932) derived an expression that gives the density of poles to platy grains as a function of deformation, assuming that the poles initially had a random distribution. Owens (1973) expanded upon the derivation with the inclusion of volume change and any initial distribution of pole densities.

The derivation of the change in pole density due to strain requires the explanation of the term solid angle. A solid angle is a measure of the amount of the field of view from some particular point that a given object covers. With this definition, the key is that the number of lines within a material cone, defining an element of solid angle, remains constant throughout deformation. Therefore, the density of poles at any angle will only change equal to the change in the solid angle. To complete this derivation, consider an initially undeformed element of solid angle, $\delta\omega_i$. For a material cone of length, D, the volume of the cone is $D^3\delta\omega/3$. The volume of the material cone can only change equal to the volumetric strain. This gives the relationship between initial and final volume to be equal to:

$$\frac{1}{3}D_i^3\delta\omega_f = \frac{1-\epsilon_{vol}}{3}D_i^3\delta\omega_f \tag{22}$$

Now with the assumption of a constant number of elements in the material cone, $f_i \delta\omega_i = f_f \delta\omega_f$, where $f_i$ and $f_f$ are the initial and final angular densities. The final angular density becomes,

$$f_f = \frac{1}{1-\epsilon_{vol}} \left(\frac{D_f}{D_i}\right)^{\frac{3}{2}} f_i. \tag{23}$$

This equation states that if I know the angular density, $f_i$, in a direction $\theta_i$before strain and if, under strain, a vector oriented along $\theta_i$ moved to $\theta_f$ then I can calculate the angular density after strain in the direction, $\theta_f$.

## APPENDIX B. DETERMINATION OF LEGENDRE COEFFICIENTS

This appendix describes the Legendre Coefficients to incorporate the alignment of grains from any strain case in the elastic stiffness prediction. The Legendre coefficients are stated as,

$$W_{lmn} = \frac{1}{4\pi^2} \int_0^{2\pi} \int_0^{2\pi} \int_0^{2\pi} W(\xi, \psi, \phi) Z_{lmn}(\xi) e^{-im\psi} e^{-in\phi} d\xi d\psi d\phi. \tag{24}$$

Where $W(\xi, \psi, \phi)$ is the generalized spherical harmonics and $Z_{lmn}(\xi)$ are the generalized Legendre functions. The limited number of coefficients needed to combine the domain elastic stiffnesses and orientation distribution function (ODF) include $W_{200}, W_{220}, W_{400}, W_{420}, W_{440}$. The generalized Legendre functions are given as (Roe, 1965):

$$Z_{lm0}(\xi) = \sqrt{\frac{2l+1}{2}\frac{(l-m)!}{(l+m)!}}P_l^m(\xi), \tag{25}$$

Where $P_l^m(\xi)$ is the Legendre polynomial of order $l$ and degree $m$. The coefficients of interest are therefore,

$$W_{200} = \sqrt{\frac{5}{2}}\int_{-1}^{1} W(\xi)P_2^0(\xi)d\xi, \tag{26}$$

$$W_{220} = \sqrt{\frac{5}{2}}\int_{-1}^{1} W(\xi)P_2^2(\xi)d\xi, \tag{27}$$

$$W_{400} = \sqrt{\frac{9}{2}}\int_{-1}^{1} W(\xi)P_4^0(\xi)d\xi, \tag{28}$$

$$W_{420} = \sqrt{\frac{9}{2}}\int_{-1}^{1} W(\xi)P_4^2(\xi)d\xi, \tag{29}$$

$$W_{440} = \sqrt{\frac{9}{2}}\int_{-1}^{1} W(\xi)P_4^4(\xi)d\xi, \tag{30}$$

With the polynomials of interest equal to,

$$\mathrm{P}_2^0 = \frac{1}{2}(3\xi^2 - 1) \tag{31}$$

$$\mathrm{P}_2^2 = 3\ (1 - \xi^2) \tag{32}$$

$$\mathrm{P}_4^0 = \frac{1}{8}\ (35\xi^4 - 30\xi^2 + 3) \tag{33}$$

$$\mathrm{P}_4^2 = \frac{15}{2}\ (7\xi^2 - 1)(1 - \xi^2) \tag{34}$$

$$\mathrm{P}_4^4 = 105\ (1 - \xi^2)^2. \tag{35}$$

## REFERENCES.


Adams, A. L., Germaine, J. T., Flemings, P. B., and Day-Stirrat, R. J., 2013, Stress induced permeability anisotropy of resedimented Boston Blue Clay: Water Resources Research, v. 49, p. 6561-6571.

Alkhalifah, T., 2000, An acoustic wave equation for anisotropic media: Geophysics, v. 65, no. 4, p. 1239-1250.

Aylmore, L. A. G., and Quirk, J. P., 1959, Swelling of Clay–Water Systems: Nature, v. 183, no. 4677, p. 1752-1753.

Backus, G. E., 1962, Long-wave elastic anisotropy produced by horizontal layering: Journal of Geophysical Research, v. 67, no. 11, p. 4427-4440.

Baker, D. W., Chawla, K. S., and Krizek, R. J., 1993, Compaction fabrics of pelites: experimental consolidation of kaolinite and implications for analysis of strain in slate: Journal of Structural Geology, v. 15, no. 9-10, p. 1123-1137.

Bandyopadhyay, K., 2009, Seismic anisotropy: Geological causes and its implications to reservoir geophysics: Stanford University.

Bayuk, I. O., Ammerman, M., and Chesnokov, E. M., 2007, Elastic moduli of anisotropic clay: Geophysics, v. 72, no. 5, p. D107-D117.

Deirieh, A., Chang, I. Y., Whittaker, M. L., Weigand, S., Keane, D., Rix, J., Germaine, J. T., Joester, D., and Flemings, P. B., 2018, Particle arrangements in clay slurries: The case against the honeycomb structure: Applied Clay Science, v. 152, p. 166-172.

Emmanuel, S., and Day-Stirrat, R. J., 2012, A framework for quantifying size dependent deformation of nano-scale pores in mudrocks: Journal of Applied Geophysics, v. 86, no. 0, p. 29-35.

Fossen, H., 2016, Structural geology, Cambridge University Press.

Han, D. h., Nur, A., and Morgan, D., 1986, Effects of porosity and clay content on wave velocities in sandstones: Geophysics, v. 51, no. 11, p. 2093-2107.

Hornby, B. E., Schwartz, L. M., and Hudson, J. A., 1994, Anisotropic effective-medium modeling of the elastic properties of shales: Geophysics, v. 59, no. 10, p. 1570-1583.

Jakobsen, M., Hudson, J. A., Minshull, T. A., and Singh, S. C., 2000, Elastic properties of hydrate-bearing sediments using effective medium theory: Journal of Geophysical Research: Solid Earth, v. 105, no. B1, p. 561-577.

Johansen, T. A., Ruud, B. O., and Jakobsen, M., 2004, Effect of grain scale alignment on seismic anisotropy and reflectivity of shales: Geophysical Prospecting, v. 52, no. 2, p. 133-149.

Jones, L. E. A., and Wang, H. F., 1981, Ultrasonic velocities in Cretaceous shales from the Williston basin: Geophysics, v. 46, no. 3, p. 288-297.

Katahara, K., 1996, Clay mineral elastic properties, SEG TECHNICAL PROGRAM, Volume In SEG Technical Program Expanded Abstracts 1996, Society of Exploration Geophysicists, p. 1691-1694.

March, A., 1932, Mathematische Theorie der Regelung nach der Korngestah bei affiner Deformation: Zeitschrift für Kristallographie - Crystalline Materials, v. 81, no. 1.

Mavko, G., Mukerji, T., and Dvorkin, J., 2009, The Rock Physics Handbook.

Morris, G. E., and Żbik, M. S., 2009, Smectite suspension structural behaviour: International Journal of Mineral Processing, v. 93, no. 1, p. 20-25.

Morris, P. R., 1969, Averaging Fourth-Rank Tensors with Weight Functions: Journal of Applied Physics, v. 40, no. 2, p. 447-448.

Nihei, K. T., Nakagawa, S., Reverdy, F., Myer, L. R., Duranti, L., and Ball, G., 2011, Phased array compaction cell for measurement of the transversely isotropic elastic properties of compacting sediments: Geophysics, v. 76, no. 3, p. WA113-WA123.

Nikolinakou, M. A., Heidari, M., Hudec, M. R., and Flemings, P. B., Stress, deformation and failure associated with salt-sheet emplacement, *in* Proceedings AGU Fall Meeting Abstracts2016, Volume 2016, p. T52C-08.

Nur, A., and Simmons, G., 1969, Stress-induced velocity anisotropy in rock: An experimental study: Journal of Geophysical Research, v. 74, no. 27, p. 6667-6674.

O'Brien, N. R., 1971, Fabric of kaolinite and illite floccules: Clays and Clay Minerals, v. 19, no. 6, p. 353-359.

Owens, W. H., 1973, Strain modification of angular density distributions: Tectonophysics, v. 16, no. 3-4, p. 249-261.

Pervukhina, M., Golodoniuc, P., Gurevich, B., Clennell, M. B., Dewhurst, D. N., and Nordgård-Bolås, H. M., 2015, Prediction of sonic velocities in shale from porosity and clay fraction obtained from logs—A North Sea well case studyPrediction of shale velocities: Geophysics, v. 80, no. 1, p. D1-D10.

Ranjpour, D., 2020, Stiffness and anisotropy characterization of mechanically-compressed cohesive soils using directional wave propagation [PhD: Tufts University.

Roe, R. J., 1965, Description of Crystallite Orientation in Polycrystalline Materials. III. General Solution to Pole Figure Inversion: Journal of Applied Physics, v. 36, no. 6, p. 2024-2031.

Sayers, C. M., 1994, The elastic anisotrophy of shales: Journal of Geophysical Research: Solid Earth, v. 99, no. B1, p. 767-774.

-, 2005, Seismic anisotropy of shales: Geophysical Prospecting, v. 53, no. 5, p. 667-676.

Sayers, C. M., Johnson, G., and Denyer, G., 2002, Predrill pore-pressure prediction using seismic data: Geophysics, v. 67, no. 4, p. 1286-1292.

Thomsen, L., 1986, Weak elastic anisotropy: Geophysics, v. 51, no. 10, p. 1954-1966.

Van Olphen, H., 1964, An introduction to clay colloid chemistry: Soil Science, v. 97, no. 4, p. 290.

Vasin, R. N., Wenk, H. R., Kanitpanyacharoen, W., Matthies, S., and Wirth, R., 2013, Elastic anisotropy modeling of Kimmeridge shale: Journal of Geophysical Research: Solid Earth, v. 118, no. 8, p. 3931-3956.

Wiggs, D. M., Flemings, P. B., Spikes, K. T., and Nikolinakou, M. A., 2020, Mudrock velocity anisotropy based on history of the full strain tensor, SEG Technical Program Expanded Abstracts 2020, Society of Exploration Geophysicists, p. 2454-2458.